European Journal of Mechanics / A Solids 121 (2027) 106300

Contents lists available at ScienceDirect

European Journal of Mechanics / A Solids

journal homepage: www.elsevier.com/locate/ejmsol

Full Length Article

Experimental characterization and phase-field modeling of crack growth in transversely graded aluminum matrix composite

Kamil Bochenek [a,1], Hossein Darban [a,1], Witold Węglewski [a], Adam Brodecki [a], Tomasz Katz [a], Ivo Dlouhy [b,c], Michał Basista [a,*]

[a] Institute of Fundamental Technological Research, Polish Academy of Sciences, Warsaw, 02-106, Poland
[b] Institute of Physics of Materials, Czech Academy of Sciences, Brno, 616 00, Czech Republic
[c] Brno University of Technology, Institute of Materials Science and Engineering, Brno, 616 69, Czech Republic

ARTICLE INFO

Keywords:
Metal-matrix composite
Multilayered structure
Nonlinear crack front
Fracture load
Stacking sequence
Phase-field modeling

ABSTRACT

Multilayered aluminum-matrix composites constitute a subclass of functionally graded materials whose mechanical properties can be systematically tailored to meet specific design requirements. In this study, experimental and numerical investigations are performed to characterize Mode I and mixed-mode I/II fracture behavior and crack growth in graded AlSi12–Al_2O_3 composites containing a notch oriented along the gradient direction. Mode I fracture tests are conducted on four-layer, disk-shaped compact specimens subjected to tensile loading, with Al_2O_3 volume fractions of 0 (pure matrix), 10, 20, and 30 percent. Crack propagation on both specimen surfaces is monitored in situ, and full-field displacement measurements are obtained using Digital Image Correlation. The experiments reveal a pronounced nonlinear crack-front propagation induced by material composition gradient along the crack front. Fracture consistently initiates in the layer with the highest content of ceramic particles, propagates within this layer, and subsequently extends into adjacent layers. Distinct fracture surface morphologies are observed using scanning electron microscopy, ranging from brittle features in ceramic-rich layers to progressively more ductile characteristics in layers with lower ceramic content. An elastic–plastic phase-field model is employed to examine the influence of stacking sequence on fracture load capacity as well as on crack-front formation and evolution under both Mode I and mixed-mode I/II loading conditions. The phase-field model is calibrated against experimentally measured fracture loads, and the characteristic length-scale parameter is identified accordingly. The simulations successfully reproduce the experimentally observed nonlinear crack-front morphology and demonstrate that the stacking sequence considerably affects the maximum load-bearing capacity and crack front geometry under both pure Mode I and mixed-mode loading.

1. Introduction

Functionally graded materials (FGMs) are created by combining two or more types of constituent materials, such as metals and ceramics, with continuously or stepwise varying compositions and properties. The goal is to obtain a versatile final material that meets the specific functional requirements of a structural component. The FGMs were introduced in the 1980s in Japan (Niino et al., 1987; Koizumi and Niino, 1995) to reduce thermal stress in aerospace applications and have since experienced sustained growth, as demonstrated in numerous review papers and books (see, for example (Neubrand and Rödel, 1997; Mortensen and Suresh, 1995; Sobczak and Drenchev, 2013; Miyamoto; Saleh et al., 2020; Gayen et al., 2019),).

From an application standpoint, the concept of using spatially varying volume fractions of metal and ceramic phases in a composite to gradually change macroscopic material properties is appealing. However, despite its conceptual simplicity, this approach poses significant technological challenges to material manufacturing, particularly for FGMs with continuous gradients (Mortensen and Suresh, 1995), as opposed to layered FGMs with stepwise grading, where compositional gradients are fully controlled during manufacturing. Moreover, the precisely designed process parameters can make the transition between

This article is part of a special issue entitled: Jean Lemaitre published in European Journal of Mechanics / A Solids.

* Corresponding author.
E-mail address: mbasista@ippt.pan.pl (M. Basista).

[1] equal contributions.

https://doi.org/10.1016/j.euromechsol.2026.106300
Received 28 February 2026; Received in revised form 16 July 2026; Accepted 18 July 2026
Available online 20 July 2026
0997-7538/

the individual composite layers almost undistinguishable (Sequeira et al., 2024). For layered metal-ceramic bulk FGMs, which are the focus of this work, the most common manufacturing techniques include powder metallurgy (Madan and Bhowmick, 2020), infiltration of molten metals into graded porous preforms (Gil et al., 2012; Maj et al., 2018), centrifugal casting (Pradeep and Rameshkumar, 2021), and additive manufacturing (Ghanavati and Naffakh-Moosavy, 2021), (Li et al., 2020).

Aluminum matrix composites (AMCs) are among the most intensively studied metal-matrix composites (MMCs) due to their unique set of properties, including high specific strength, stiffness, hardness, and wear resistance (e.g. (Basista et al., 2017),). Consequently, the AMCs have found extensive application in a variety of domains, including aerospace, automotive, and defense sectors (Chak et al., 2020). An interesting representative of the AMCs class is a composite where an Al matrix is reinforced with alumina (aluminum oxide, Al_2O_3). In this case, there is no thermodynamic incompatibility between the aluminum matrix and the alumina reinforcement. Furthermore, no solubility of one phase in another is observed, which results in enhanced interfacial bonding between the aluminum matrix and the alumina reinforcing particles (Pandey and Patel, 2020). This, in turn, positively impacts the mechanical properties of the Al–Al_2O_3 composites, which is crucial for structural applications. Among the mechanical properties of a structural material intended for use under mechanical loading, the fracture parameters, such as stress intensity factors, energy release rate, and J-integral, as well as crack growth patterns, are of particular interest, as they reflect material's response to mechanical loading and determine its suitability for engineering applications. Given the composition gradient of the FGMs, it was reasonable to assume that their fracture parameters would differ from those of homogeneous materials. However, several works have demonstrated that the asymptotic stress field at the crack tip is characterized by the inverse square root singularity, provided that the property gradient is continuous and piecewise differentiable (Jin and Noda, 1994), (Parameswaran and Shukla, 2002). After this finding was widely accepted, a lot of research effort went into determining stress intensity factors (SIFs) for the FGMs. For example, the SIFs were numerically determined by the finite element method (FEM) for a graded plate with an edge crack, assuming an exponential distribution of Young's modulus (Anlas et al., 2000). Other examples of numerical evaluations of SIFs for FGMs include the use of the extended finite element method (XFEM) (Dolbow and Gosz, 2002) and the boundary element method (Zhang et al., 2011).

Analytical and numerical works on the fracture of the metal-ceramic FGMs are extensive, while experimental studies on the subject are scarce. However, a notable exception to this general trend is represented by a series of experimental studies undertaken to investigate the fracture parameters and crack growth trajectories in a specific material system, namely multilayered Ti/TiB FGMs. Kidane and Shukla (2010) studied the fracture initiation process in seven-layer Ti/TiB FGMs under three-point bending using single-edge notched bend (SENB) specimens. They placed particular emphasis on the effects of temperature and loading rate on quasi-static and dynamic fracture initiation. The analysis encompassed two cases of notch orientation: (i) perpendicular to the gradient direction, and (ii) parallel to the gradient direction. In the first case, the fracture toughness remains constant along the fracture front. In the second case, however, it varies along the fracture front due to the transverse layer stacking, which complicates the analysis of FGM fracture (Wadgaonkar and Parameswaran, 2009a). Sahragard-Monfared et al. (2023) investigated the microstructural toughening mechanisms in the seven-layer Ti/TiB graded specimens under three-point bending with a notch placed orthogonally to the gradient direction. Their analysis revealed crack bridging by the Ti ligaments, crack deflection around TiB particles, and crack branching, resulting in an increasing R-curve behavior. Kohboor et al. (Koohbor et al., 2019) examined the fracture behavior of seven-layer Ti/TiB FGMs under uniaxial tension, with the pre-crack oriented parallel to the gradient direction ("transversely graded material"). They used Digital Image Correlation (DIC) with two CCD cameras to simultaneously determine the full displacement fields on both sides of the specimen.

Research works (Kidane and Shukla, 2010) and (Sahragard-Monfared et al., 2023) have demonstrated that, for multilayered Ti/TiB FGMs with pre-cracks in the TiB-rich side oriented orthogonally to the gradient direction, the crack front is straight, indicating a mode I fracture. Distinct peaks were recorded on the load-time plot corresponding to the cracking of subsequent layers. Crack growth was stable and exhibited crack arrest effects. SEM analysis in study (Sahragard-Monfared et al., 2023) revealed no interaction between the growing crack and ceramic particles up to the layer with a TiB volume fraction of nearly 50%. The crack observed by SEM remained planar and generally perpendicular to the tensile load direction. However, as the crack propagated toward the Ti-rich side, matrix ductility began to play a more significant role, inducing the cracking of TiB particles and debonding from the Ti matrix.

In transversely graded Ti/TiB FGMs, non-uniform crack growth occurred as the stress intensity factor on the TiB-rich side reached fracture toughness (Kidane and Shukla, 2010), (Koohbor et al., 2019). The crack front propagated from the TiB-rich side toward the Ti-rich side, manifesting a curvilinear contour. According to the fractography analysis presented in (Kidane and Shukla, 2010), the fracture surface near the TiB side was smooth, indicating a brittle fracture. In contrast, the fracture surface near the Ti-rich side was rough, suggesting a more ductile fracture.

This research aims to investigate crack growth in Al-matrix FGMs with a transverse gradient under tensile loading. The topic will be studied through both experimental methods and phase-field modeling. According to a literature review, crack propagation in transversely graded Al-matrix FGMs has not been systematically evaluated in standard fracture tests, nor has phase-field modeling been used for this purpose. This study intends to address this research gap.

2. Experiment

2.1. Processing of the AlSi12–Al_2O_3 graded composite (FGM)

The functionally graded material, which was the subject of this study, was a step-wise graded composite (FGM) consisting of multiple layers made of an AlSi12 alloy matrix strengthened with alumina (Al_2O_3) particles of varying amounts. For the experimental examination and phase-field modeling of crack growth, it was assumed that a four-layer FGM, AlSi12 + x Al_2O_3, where x = 0, 10, 20, and 30 vol%, would be sufficiently representative. The AlSi12 alloy was selected as the matrix due to the increasing use of aluminum-silicon alloys in the automotive sector, which is targeted as a potential user of this AlSi12 + x Al_2O_3 graded composite as a material for brake discs. In the assumed layer arrangement of the FGM, the outer layer, which contains a high concentration of alumina particles, is expected to enhance wear resistance during car braking. The inner layers of the FGM, which contain a lower Al_2O_3 content, will provide the mechanical strength required for the brake disc.

The AlSi12 powder delivered by NewMetKoch had an average as-received particle size of 4.6 μm and a purity of 99.99%. The Si content of 12.1 vol% of this powder exhibited a close correspondence to the EN AC–44200 grade, which is a standard cast aluminum alloy that is widely used in various industries (Gitter, 2008). The ceramic reinforcement used in the FGM manufacturing process was a commercial Al_2O_3 powder produced by Goodfellow. This powder exhibited an average as-received particle size of 5.3 μm and 99.99% purity. The particle-size distributions of the two powders in their as-received state were determined using a Malvern Mastersizer 3000 equipped with a HydroMV2000 dispersion unit. Further information on the morphology of the starting powders are provided in (Sequeira et al., 2024) and (Sequeira et al., 2026).

The starting powders were blended in a Fritsch Pulverisette 5 planetary ball mill, using 250-ml bowls and 10-mm balls, both made of tungsten carbide. Milling was conducted at a rate of 100 rpm with a ball-to-powder weight ratio of 5:1 for a total duration of 5 h. The milling intervals were set at 15 min, with 45-min pauses between each interval to prevent overheating. All powder handling and vial sealing were conducted in an inert-atmosphere glove box to suppress oxidation. Heptane was used as the milling medium to enhance dispersion and restrict agglomeration. The resultant suspension was then subjected to vacuum-drying to eliminate residual solvent.

Layer-specific powder masses for the FGM (AlSi12 + x Al_2O_3, where x = 0, 10, 20, 30 vol%) were calculated from the theoretical density and weighed accordingly to achieve the target layer thicknesses (approx. 1.5 mm for each layer). Green compacts were formed by uniaxial cold pressing at 100 MPa in a steel mould, with a 30s holding time. The individual layers were sequentially stacked in a graphite mould to ensure an arrangement consistent with the designed functionally graded material. Due to the use of graphite foil interlayers during sintering, the outer layers (pure AlSi and AlSi + 30% Al_2O_3) were made thicker in order to allow, through machining, the production of a finished functionally graded composite with a final thickness of 6 mm. Hot-pressing (HP) was carried out in vacuum using a graphite mould at 560 °C with a heating rate of 5 °C/min, a dwell time of 180 min, and an applied pressure of 30 MPa. The sintering temperature of 560 °C in the HP, which was slightly below the AlSi12 solidus temperature (~590 °C), promoted near-complete densification via solid-state diffusion while preventing matrix melting. The ungraded composites with 10, 20 and 30 vol%Al_2O_3 were manufactured using the same powder metallurgy route as the layered composite (FGM). This process included powder mixing, cold compaction, and hot pressing, all under identical conditions as the FGM. The only difference was that the powders were introduced as a single batch rather than in multiple layers. The relative densities of ungraded composites exceeded 99% (Table 1). Additional information regarding the distribution of pore sizes in composite layers of the FGM can be found in our previous study (Sequeira et al., 2024).

2.2. Microstructural characterization

The microstructure of the AlSi12–Al_2O_3 composite layers was analyzed to assess the distribution of the ceramic reinforcement, the quality of the matrix–particle interfaces, and the overall integrity of the consolidated material. Before the SEM examination, the samples were ground and polished to a 1-µm finish using a diamond suspension in a Presi Mecatech 334 device. Microstructural observations of the individual layers of the FGM were performed using a ZEISS Crossbeam 350 scanning electron microscope (SEM) equipped with a secondary-electron detector operating at 5 kV (Fig. 1. 1a–d).

The SEM examination revealed that the Al_2O_3 particles were uniformly dispersed within the AlSi12 matrix with no indication of significant agglomeration or clustering. The ceramic particles had clean, well-defined interfaces with the metallic matrix. This suggests that densification and diffusion bonding occurred effectively during sintering. The hot pressed composites showed a dense and homogeneous microstructure with minimal residual porosity. These high densification levels, together with the observed microstructural uniformity due to random Al_2O_3 particles distribution, demonstrate the stability and compatibility of Al_2O_3 as a reinforcing phase in AlSi12 alloys, underscoring the suitability of these composites for thermally demanding structural applications.

Table 1
Average sizes of alumina grains in AlSi12 + 10 vol%Al_2O_3, AlSi12 + 20 vol% Al_2O_3, and AlSi12 + 30 vol%Al_2O_3 composite samples.

Composite	Number of analyzed particles	Mean ECD (2D) [µm]	Dv10 [µm]	Dv50 [µm]	Dv90 [µm]
AlSi12 + 10% Al_2O_3	822	1.95	2.58	5.64	9.24
AlSi12 + 20% Al_2O_3	1347	1.91	2.75	5.94	10.39
AlSi12 + 30% Al_2O_3	5960	1.98	2.74	6.19	10.47

The average grain size of the AlSi12 matrix after hot pressing, determined according to ASTM E112 (ASTM E112-96, 2004), was approximately 4.3 µm. The average size of the Al_2O_3 particles (5.3 µm) in the as-received state did not change significantly during the preparation of the powder mixture and the consolidation of the composite samples by hot pressing. SEM observations (Fig. 1b–d) confirmed that the alumina particles retained their original morphology and remained uniformly distributed throughout the matrix, with no evidence of fragmentation, agglomeration, or particle coarsening. To verify these observations, a quantitative image analysis was performed on representative SEM micrographs using ImageJ software (Schneider et al., 2012). The equivalent circular diameters (ECD) of more than 8000 particles in total were determined, and the corresponding volume-equivalent particle size distribution was calculated assuming spherical particles. As can be seen from Table 1, the obtained Dv50 values ranged from 5.6 to 6.2 µm, which is in relatively good agreement with the average particle size of the as-received Al_2O_3 powder measured by laser diffraction. The slight differences can be attributed to the different measurement methods employed. Specifically, laser diffraction provides a true three-dimensional volume-equivalent particle size distribution based on Mie scattering theory, whereas image analysis is based on two-dimensional polished cross-sections.

It should be emphasized that according to SEM observations, the continuous phase remained the AlSi12 matrix in all investigated materials, irrespective of the alumina content. Consequently, the observed differences in fracture behavior reported in Section 2.5 cannot be attributed to changes in the matrix phase itself, but rather to the increasing fraction of discontinuous Al_2O_3 reinforcement. The higher ceramic content reduces the effective volume of the ductile matrix available for plastic deformation and increases the density of particle–matrix interfaces, which act as preferential sites for stress concentration, crack initiation and crack path modification. As a result, fracture behavior is increasingly controlled by reinforcement-induced mechanisms rather than by changes in the intrinsic properties of the matrix.

2.3. Elastic constants

The Young's modulus and Poisson's ratio of the FGM constituent layers were measured using the pulse-echo method, an ultrasonic technique that enables precise evaluation of the elastic constants by measuring the propagation velocities of longitudinal and transverse ultrasonic waves within the specimen. The generation and detection of ultrasonic pulses were carried out using a Panametrics Epoch 4 ultrasonic flaw detector, remotely controlled by a personal computer equipped with dedicated software for accurate determination of the ultrasonic pulse time-of-flight. The nominal frequencies of the transducers were 10 MHz for longitudinal waves and 5 MHz for transverse waves. The tested specimens were prismatic bars with a square cross-section of $3 \times 4\ mm^2$. Ultrasonic wave velocities were measured along two mutually perpendicular directions within the cross-section of each specimen. The Young's modulus (E) and Poisson's ratio (ν) calculated under the assumption of material isotropy are presented in Table 2. Additionally, the density of the materials that compose the FGM was measured using Archimedes' method. Then, the relative densities were determined based on the measured data and the theoretical densities (see Table 2).

2.4. Tensile tests

Tensile tests of the AlSi12 matrix alloy and the AlSi12 + 10%Al_2O_3 and AlSi12 + 30%Al_2O_3 composites were performed using a Zwick Z050

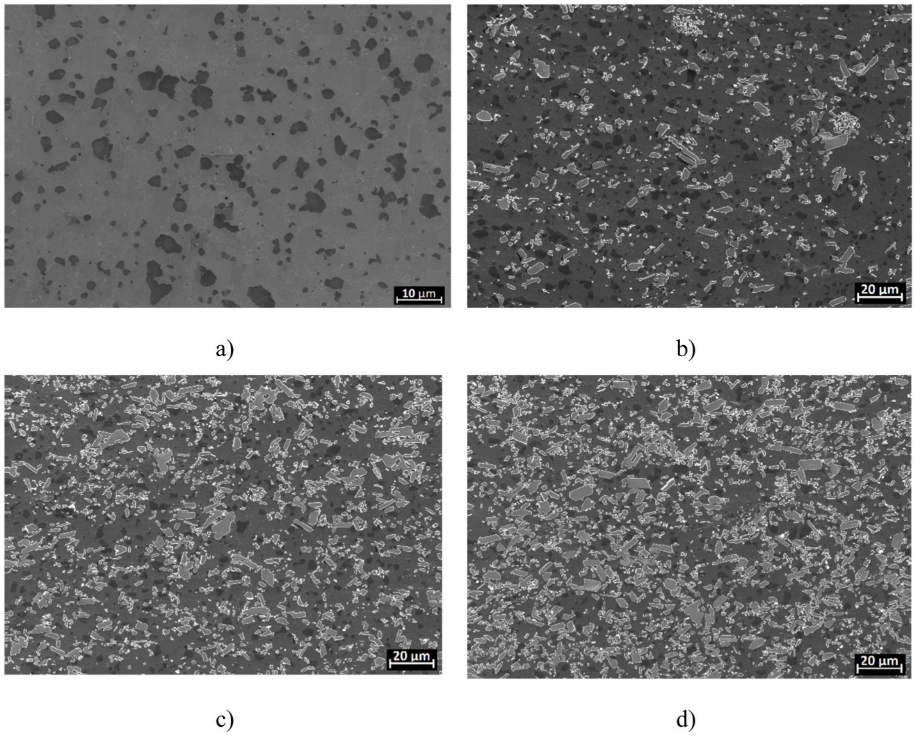

Fig. 1. Microstructure of the individual layers of the FGM: a) AlSi12, b) AlSi12 + 10%Al_2O_3, c) AlSi12 + 20%Al_2O_3, d) AlSi12 + 30%Al_2O_3. The black spots visible in Fig. 1(a–d) are Si grains surrounded by the Al matrix.

Table 2
Elastic constants of the manufactured materials measured by the pulse-echo method.

Material	Young's modulus (E) [GPa]	Poisson's ratio (ν)	Relative density [%]
AlSi12	79.7	0.34	99.94
AlSi12 + 10% Al_2O_3	92.4	0.33	99.68
AlSi12 + 20% Al_2O_3	110.2	0.31	99.81
AlSi12 + 30% Al_2O_3	125.2	0.30	99.61

universal testing machine to provide input parameters for numerical modeling. Dog-bone–shaped tensile specimens were prepared by wire electrical discharge machining (Mitsubishi MV1200R) and subsequently polished. Uniaxial tensile tests were conducted at room temperature at a strain rate of 0.1 mm/min, and the resulting stress–strain curves are shown in Fig. 2. The mechanical response of the intermediate composite layer (AlSi12 + 20%Al_2O_3), for which experimental data were unavailable, is not shown in Fig. 2.

From the tensile test records (Fig. 2) and the parameters evaluated from them, a significant difference in the values of uniform elongation – the strain corresponding to the plastic instability limit, localized at the maximum force (stress) on the loading curve – is evident. Uniform elongation ranges from 5.3% to 6.3% for 10 vol% content, compared to 1.7% to 1.9% for 30 vol% Al_2O_3 fraction in the AlSi12 matrix. For a composite with 10% Al_2O_3 particles, this elongation can be associated, similarly to the matrix without Al_2O_3 particles, with plastic deformation only, while for composites with 30% particle fraction, the localization of deformation is accelerated, leading to earlier damage onset followed by premature fracture.

2.5. Specimen preparation and fracture testing of composite layers and FGM

The fracture toughness of the FGM constituent materials was measured using single-edge V-notched beam specimens (SEVNB) in four-point bending mode according to ISO standard 23,146 (ISO 23146 Advanced Technical Ceramics, 2015). From the sintered samples, prismatic specimens of the following dimensions 25 x 4 × 3 mm^3 were cut by wire cutter (Mitsubishi MV1200R). The notches, as described in (ISO 23146 Advanced Technical Ceramics, 2015), were machined by a notching machine using a razor blade and diamond paste up to 1 µm particle size. This method was previously validated in a parallel study conducted on a similar type of composite (Bochenek et al., 2025). ASTM E399 (ASTM E399, 2022) recommends fatigue pre-cracking to ensure a sharp crack tip. However, the adopted notch preparation method was the most reliable and reproducible approach for the layered composite system under investigation, ensuring high notch straightness and geometric reproducibility. A similar method of preparing notches based on machining rather than pre-cracking due to fatigue has also been employed for layered and functionally graded composites, including the Ti–TiB graded materials investigated by Koohbor et al. (2019). Stable fatigue crack growth was also difficult to achieve in these materials due to their heterogeneous microstructure. The fatigue pre-cracking generally provides the sharpest crack tip and may lead to more conservative fracture toughness values, as required by ASTM E399 (ASTM E399, 2022). Furthermore, previous studies have demonstrated that notch sharpness can influence the measured fracture toughness values, particularly the crack-initiation toughness. For example, Moore et al. (Moore, 2014) reported that EDM notches may result in higher crack-initiation toughness values compared with fatigue-precracked specimens. Nevertheless, the same study demonstrated that the overall fracture resistance behavior and crack propagation mechanisms remained qualitatively similar. Therefore, while the K_{Ic} values may be affected by notch acuity, the comparative assessment of crack propagation mechanisms and the influence of the layered architecture remains

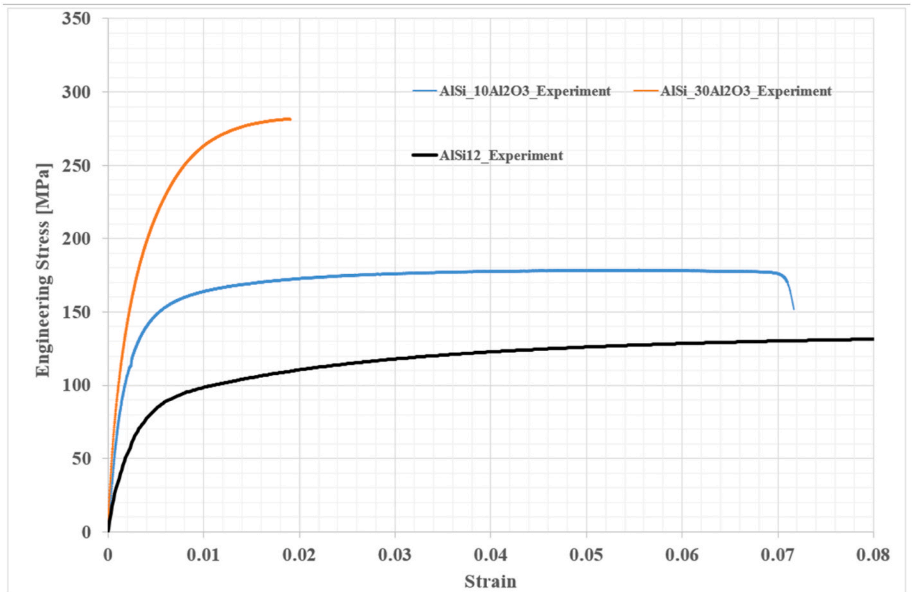

Fig. 2. Experimental stress-strain curves for the unreinforced AlSi12 matrix, AlSi12 + 10%Al_2O_3, and AlSi12 + 30%Al_2O_3 composites in uniaxial tension.

valid.

Table 3 shows the fracture toughness values obtained for the AlSi12 matrix and the AlSi12–Al_2O_3 composites that were sintered by hot pressing. It should be noted that, except for the matrix itself – that is, the AlSi12 alloy without Al_2O_3 particles – the composites met the LEFM conditions prescribed by the relevant standards (ASTM E399, 2022; ASTM E 1820, 2001). Five specimens were tested for each composition that is the AlSi12 matrix and the three composites. The AlSi12 matrix exhibited the highest average K_{IC}, at 12.82 ± 0.07 MPa·$\sqrt{\text{m}}$. Incorporating 10 vol% Al_2O_3 resulted in a slight reduction of K_{IC}. However, the addition of 20 and 30 vol% Al_2O_3 led to a significant decrease in fracture toughness. There is an evident correlation between the K_{IC} values in Table 3 and the decreasing relative density of the composite samples, as shown in Table 2.

Fig. 3 presents the SEM images of the fracture surfaces of the AlSi12 matrix and the AlSi12–Al_2O_3 composites after the bending test. The presence of dimples (Fig. 3a) at the interfaces between the ductile aluminum and brittle silicon particles indicates a ductile type of fracture in the AlSi12 matrix. In the composite specimens (Fig. 3b–d), the ductile fracture of the AlSi12 matrix is accompanied by brittle cracking of alumina particles and debonding from the matrix.

Fracture tests were conducted on the four-layer, transversely graded FGM using disc-shaped compact specimens under tensile loading. The ASTM E 1820 standard (ASTM E 1820, 2001) permits the use of disc-shaped compact specimens. This was advantageous in this study, as the sintered FGM samples were also discs. However, the ASTM E 1820 standard proportions and dimensions could not be fully met due to the technical limitations of the hot press used in this study. Consequently, the specimen shown schematically in Fig. 4 is a customized, compact disc-shaped specimen. The preparation of the FGM test specimens consisted of the following steps. First, the sintered FGM discs were ground from both sides to a thickness of approximately 6 mm to maintain an equal thickness of the compact tension specimen. The specimen depicted in Fig. 4 was machined using a wire cutter. Due to the intricate nature of the FGM and a nonuniform distribution of material properties along the notch, the fatigue precracking according to the ASTM E399 standard (ASTM E399, 2022) was not applied. Instead, a sharp notch was obtained by the same procedure as for the SEVNB specimens, after customizing the notching machine for the compact tension specimens. After this step, the specimen surfaces were polished using a Presi Mecatech 334. The notches were characterized by their depth and diameter (Table 4).

Table 3
Fracture toughness of the composite layers in SEVNB probe under four point bending.

Material	Fracture toughness K_{IC} $[MPa\sqrt{m}]$
AlSi12	12.82 ± 0.07
AlSi12 + 10%Al_2O_3	12.40 ± 0.81
AlSi12 + 20%Al_2O_3	9.22 ± 0.82
AlSi12 + 30%Al_2O_3	8.75 ± 0.54

Upon analyzing the notch geometric data in Tables 4 and it is evident that the notches are inclined in one direction, with the exception of Specimen 4. This is related to the way the specimens were machined and notched, and does not follow any systematic trend related to material architecture. The notch inclination of Specimen 4 differs from that of the other test specimens and represents normal experimental scatter associated with the manual notch preparation procedure. Since all specimens satisfied the geometric requirements of the testing methodology in ISO 23146 (ISO 23146 Advanced Technical Ceramics, 2015), no measurable influence on the reported fracture toughness values was observed.

Fig. 5 shows the SEM image of the notch tip from both sides of the FGM compact specimen.

2.6. Crack growth in disc-shaped compact specimens of transversely graded FGM

The FGM samples consisted of four layers, AlSi12, AlSi12 + 10% Al_2O_3, AlSi12 + 20%Al_2O_3, and AlSi12 + 30%Al_2O_3, stacked in this order across the specimen thickness. The tension tests were performed on an MTS 858 universal testing machine equipped with compact-specimen grips and 6 mm diameter loading pins. A constant crosshead displacement rate of 0.01 mm/s was applied. Digital image correlation (DIC) measurements were conducted using an Aramis 12 system positioned on the AlSi12 side of the specimen to monitor crack evolution and to obtain the actual displacement during loading. Prior to the DIC testing, the specimen surface was degreased and thoroughly cleaned. A uniform white primer layer was then applied. After the white coating had dried, a random speckle pattern was created using an airbrush and black paint. The paint used for the speckle pattern was matte, and the applied layers were kept as thin as possible to avoid disturbing the

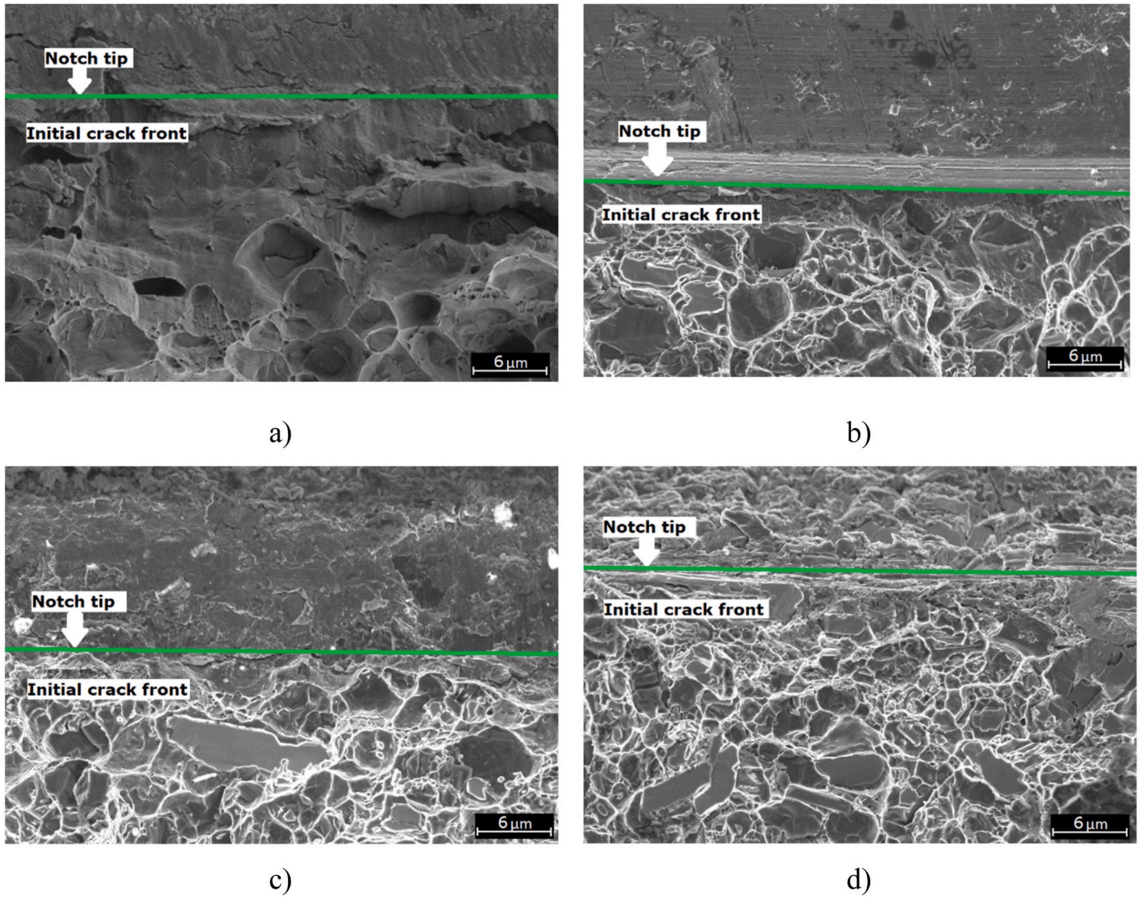

Fig. 3. SEM images of fracture surfaces of the materials used in the FGM: a) AlSi12, b) AlSi12 + 10%Al_2O_3, c) AlSi12 + 20%Al_2O_3, d) AlSi12 + 30%Al_2O_3.

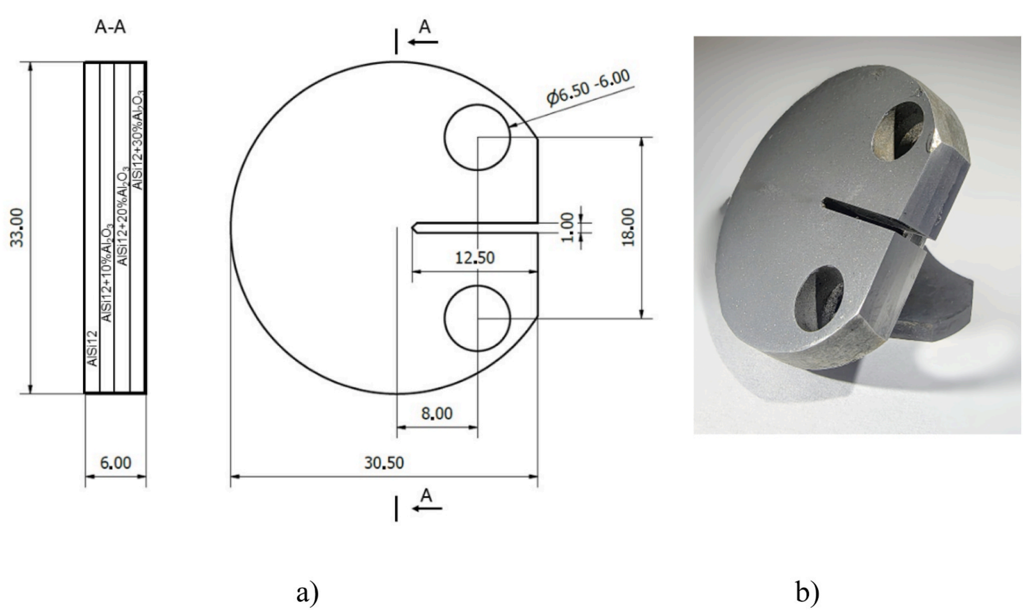

Fig. 4. Disc-shaped compact tension specimen made of four composite layers with 0%Al_2O_3 10%Al_2O_3, 20%Al_2O_3, and 30%Al_2O_3: a) Dimensions of the specimen (mm); b) Photograph of the specimen used in fracture tests.

displacement measurements on the specimen surface. Owing to the high sensor resolution (12 MP; 4096 × 3000 px) and system limitations, the acquisition frequency was set to 2 Hz, with a field of view of 50 × 70 mm. On the opposite side, corresponding to the counter-layer (AlSi12 + 30% Al_2O_3), a high-speed optical system was used to record crack propagation ahead of the crack tip. The high-speed setup consisted of a Keyence VW-9000 microscope coupled with a Keyence VW-600C high-speed camera. To capture the rapid crack growth events originating at

Table 4
Depths and diameters of the notches machined by a customized notching machine with a razor blade.

Specimen	AlSi12 side		$AlSi12 + 30\%Al_2O_3$ side		Fracture load [N]
	Notch depth [μm]	Notch diameter [μm]	Notch depth [μm]	Notch diameter [μm]	
1	145.8	28.99	179.9	21.32	2315.31
2	64.33	26.36	141.8	40.79	2620.76
3	58.74	20.26	165.3	18.83	2147.75
4	183.4	22.40	138.4	24.53	2034.78

the notch, the camera operated at 60 fps with an image resolution of 640 × 320 px. The primary limitation of this configuration is the reduced field of view, which is restricted to the inner region of the specimen. Fig. 6 shows the complete experimental setup.

During the loading process, crack propagation was initiated and rapidly advanced through the stiffer and more brittle AlSi12 + 30% Al_2O_3 layer, leading to complete fracture of that specimen. In contrast, the crack had only begun to emerge within the pure AlSi12 layer on the opposite side when the test was halted, reflecting the pronounced gradient in fracture resistance across the FGM architecture. Similar non-uniform fracture process in transversely graded FGMs was reported for Ti/TiB FGMs by Kidane and Shukla (2010) in three-point bending, and Kohboor et al. (Koohbor et al., 2019) for Ti/TiB FGMs in uniaxial tension on prismatic specimens.

Fig. 7 shows the load-displacement curve derived from the tension test of the compact, disk-shaped FGM specimen. The images from the Keyence camera and the DIC Aramis system, included in this figure, illustrate the progression of crack growth at selected stages of the loading process.

Inset A of Fig. 7 shows the initial state of the two sides of the notched FGM test specimen at different magnifications. Images taken at maximum force (point B) during the loading process reveal a visible crack on the AlSi12 + 30%Al_2O_3 side, but no crack on the pure AlSi12 matrix side. At point C, a well-developed crack propagates through the AlSi12 + 30%Al_2O_3 layer, while crack initiation is observed on the pure matrix side. Finally, the images corresponding to point D of the force-displacement curve show cracks on both sides of the specimen.

Fig. 8 presents the fracture surface of the compact FGM specimen after partial cracking during the tension test. Because the specimen did not fully separate during testing, after the test it was immersed in liquid nitrogen and manually fractured to expose the complete fracture surface without introducing thermal or plastic deformation artefacts. This

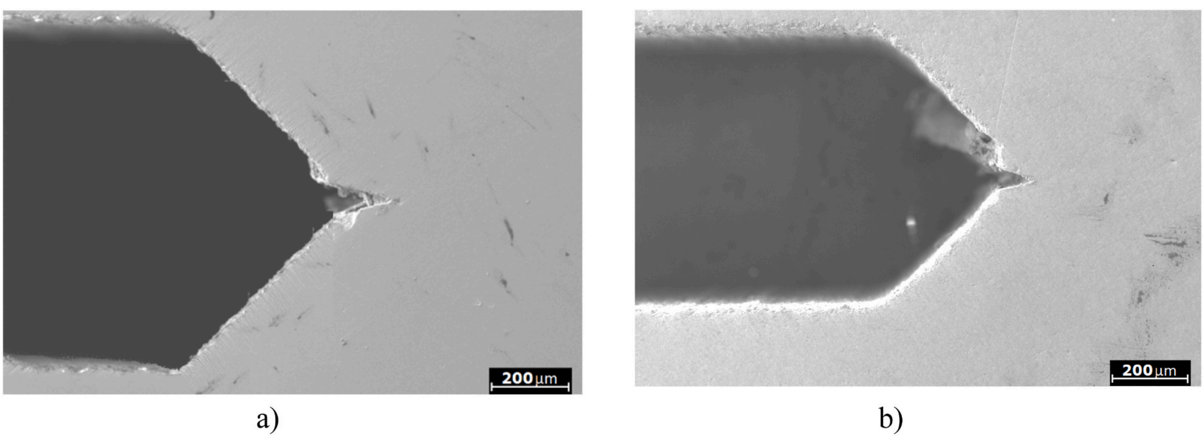

Fig. 5. SEM images of the notch tip machined with the customized notching machine using a razor blade: a) the AlSi12 side of the FGM, b) the AlSi12 + 30%Al_2O_3 side of the FGM.

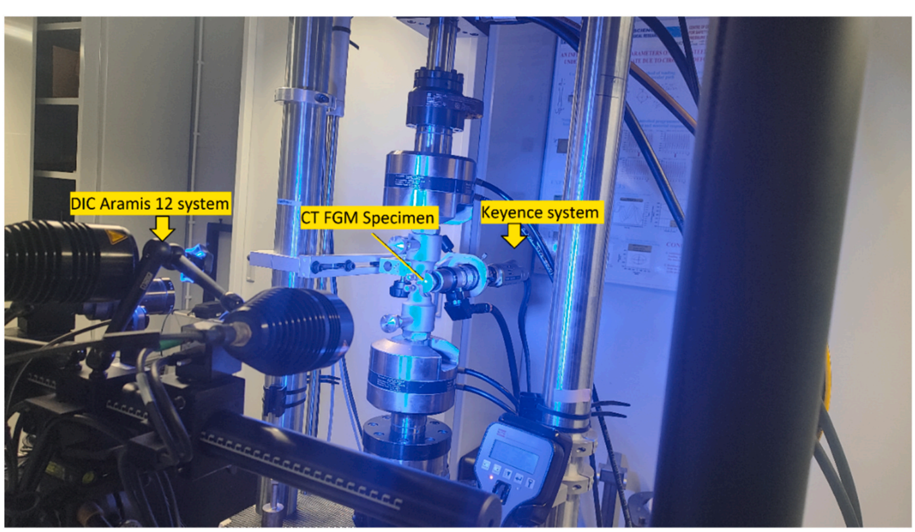

Fig. 6. The experimental setup used to evaluate crack growth in a transversely graded AlSi12–Al_2O_3 compact specimen. The disc-shaped FGM specimen is mounted in the center. The DIC Aramis 12 system is positioned in front to measure displacements on the AlSi12 side. The Keyence high-speed camera is positioned on the AlSi12 + 30%Al_2O_3 side of the FGM specimen to observe crack growth.

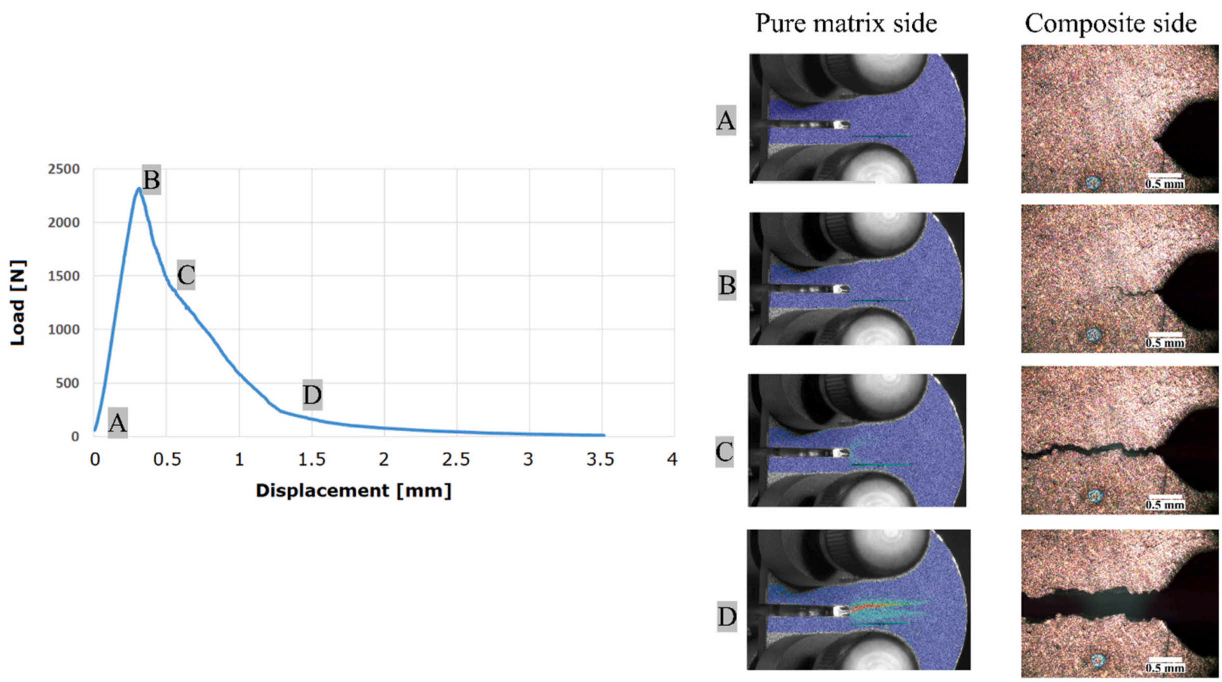

Fig. 7. The load-displacement curve derived from the tension test using the compact disk-shaped FGM specimen. Images captured from the Keyence camera (composite side, AlSi12 + 30%Al_2O_3) and the DIC Aramis system (pure matrix side, AlSi12) illustrate the gradual crack growth at selected stages of the loading process (A, B, C, D).

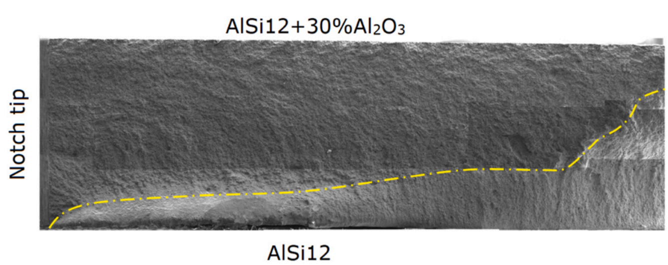

Fig. 8. A combined image of a series of SEM micrographs showing the fracture front in the transversely graded AlSi12–Al_2O_3 FGM specimen. The disk-shaped C-T specimen did not fracture during the test. The fracture surface shown in the figure was obtained by immersing the partially fractured FGM specimen in liquid nitrogen. The dimensions of the image shown are approximately 18.5 mm × 6 mm.

ensured that the intrinsic fracture morphology of each graded layer could be examined. The SEM image in Fig. 8 is a stitched image of 45 SEM micrographs, providing a continuous panoramic view of the fracture zone. The fractured surface clearly reveals the transition in fracture mechanisms across the four material layers. The AlSi12 + 30% Al_2O_3 region exhibits a highly rough and irregular topography characteristic of brittle fracture governed by particle–matrix decohesion and limited plasticity. Moving toward the intermediate layers (10% and 20% Al_2O_3), the surface morphology becomes progressively less tortuous, reflecting the gradual reduction of ceramic reinforcement and the increasing ability of the matrix to plastically deform. Finally, in the pure AlSi12 layer, the fracture surface becomes smoother and ductile tearing features, consistent with delayed crack initiation and higher energy absorption compared to the ceramic-rich layers.

Overall, the panoramic SEM image highlights the strong correlation between local reinforcement content and crack behavior in the FGM. Increasing the Al_2O_3 content promotes brittleness and accelerates crack propagation, while lower ceramic fractions and the unreinforced AlSi12 layer exhibit more ductile fracture modes.

3. Phase-field modeling of crack growth in transversely graded FGM

The phase-field modeling approach reformulates the fracture problem as an energy minimization problem. In this method, the sharp crack discontinuity is approximated by a diffuse topology using an exponential regularization function with a length scale and a phase-field variable d. The parameter $d = 0$ corresponds to intact material regions far from any crack, while d gradually increases toward the crack surface, reaching $d = 1$ in fully fractured zones. Since this formulation does not require an explicit geometric description of the crack, it avoids the need for discretization and ad hoc criteria for crack initiation and propagation that are commonly required in discrete fracture models such as the cohesive zone models. As a result, complex fracture phenomena can be captured naturally by energy minimization.

There are several advanced phase-field models for fracture in FGMs with spatially continuous material property gradations. One of the earliest models was developed in (Doan et al., 2016) to study dynamic crack propagation in FGMs. The authors showed that the phase-field modeling predictions of crack trajectory and velocity are in agreement with experimental data. Similarly, crack branching in FGMs under impact loading was studied in (Dinachandra and Alankar, 2020) using a phase-field model. In (Asur Vijaya Kumar et al., 2021), a phase-field fracture model was developed for FGMs where the length scale parameter also has a spatial variation, resembling the spatial variation of the material strength. Other examples include the phase-field method utilized in (Dsouza et al., 2021) to study fracture in FGMs with random material properties, and the electro-mechanically coupled phase-field modeling of fracture for functionally graded piezoelectric ceramics presented in (Mohanty et al., 2020).

In this section, the phase-field method is employed to investigate elastic–plastic fracture in disc-shaped compact tension specimens, as tested in Section 2. The numerical simulations aim to understand the influence of layer stacking sequence on the fracture response of these specimens under mode I and mixed-mode I/II loading. Since the material gradation is step-wise rather than continuous, we do not employ a phase-field model with continuous spatial property variations. Instead, we model the specimens as a four-layer system, in which each layer is treated as an isotropic homogeneous material with effective properties. All simulations are performed using the open-source Abaqus implementation of the phase-field formulation presented in (Molnár et al., 2020). The implementation employs a linear hardening plasticity model based on the von Mises yield criterion, with the constitutive parameters derived directly from experimental data. This approach ensures the model adequately captures the underlying physics of the composite, since macroscopic failure in layers containing a low volume fraction of ceramic reinforcement is predominantly governed by matrix yielding and plastic deformations before fracture. The numerical solution is obtained using an implicit staggered finite element scheme, and additional details are provided in the original publication (Molnár et al., 2020). For the sake of completeness, the model and its numerical implementation are briefly summarized in Appendix A.

The simulations require several input parameters for each layer, including the Young's modulus, Poisson's ratio, yield strength, hardening modulus, critical strain (defined as the strain at which the material totally breaks), fracture energy, and the length scale l_c. Except for the length scale, all input parameters listed above are reported in Table 5. The length scale parameter will be calibrated in Section 3.1 by fitting the numerically predicted fracture load to the corresponding experimental measurement.

The Young's moduli and Poisson's ratios are measured by the pulse-echo method, as described in Section 2.3 and reported in Table 2. The yield strength, hardening modulus, and critical strain of AlSi12, AlSi12 + 10%Al_2O_3, and AlSi12 + 30%Al_2O_3 are obtained from the experimental stress–strain curves shown in Fig. 2. The yield strength, hardening modulus, and critical strain of AlSi12 + 20%Al_2O_3 are assumed such that their values fall between those of AlSi12 + 10%Al_2O_3 and AlSi12 + 30%Al_2O_3. The fracture energy is calculated from the fracture toughness values reported in Table 3 and the corresponding Young's modulus using the relation $G_c = K_{IC}^2/E$.

The simulations are performed using eight-node, three-dimensional brick elements with linear interpolation of all field variables. The mesh employed to discretize the domain is shown in Fig. 9, with a detailed view of the region near the crack tip provided in the inset. The details regarding the crack geometry and dimensions are presented in Appendix B. The mesh size decreases linearly from 250 μm at a distance of 1 mm from the crack tip to 2 μm in the immediate vicinity of the crack tip. Two elements are used to discretize each layer through the thickness. To maintain computational efficiency, a mesh size of 2 mm is used in regions far from the crack tip. The simulations involve more than 16,000 finite elements. The displacement is applied to the nodes located on the surfaces of the loading holes with a rate of 5×10^{-7} mm/step, and the corresponding reaction force is recorded throughout the simulations.

The in-plane mesh size in the regions near the initial crack tip (2 to 250 μm) is sufficiently fine to resolve the damage zone and accurately capture crack initiation and propagation. However, the out-of-plane mesh size (two elements per layer) represents a relatively coarse discretization that requires verification. To address this, a convergence study was conducted by simulating models with four and six elements per layer. The results, presented in Fig. C1 of Appendix C, demonstrate that the maximum load sustained by the specimen and the crack trajectory do not change significantly with further transverse refinement. This confirms that a discretization of two elements per layer is sufficient for the scope of this work. While a higher transverse mesh resolution would allow a more precise investigation of the local crack front geometry, such simulations incur prohibitive computational costs. Therefore, the computationally efficient discretization of two elements per layer is employed throughout the remainder of this section.

All computations are carried out on the Ares supercomputer hosted by the Academic Computer Center CYFRONET AGH in Kraków, Poland. A single computing node equipped with 48 cores from dual Intel Xeon Platinum 8268 processors (2.90 GHz) and 192 GB of RAM is employed. The total wall-clock time required for each simulation is approximately 40 h.

3.1. Phase-field modeling

The only remaining modeling parameter that requires identification is the phase-field length scale parameter. In the literature, this parameter is treated either as an arbitrary numerical regularization length or as a physical material property that must be calibrated experimentally (Nguyen et al., 2016). Experimental calibration strategies can generally be classified into global and local approaches. Global approaches utilize macroscale structural responses, such as the ultimate strength or peak fracture load, to calibrate the length scale (Zhang et al., 2017; Tanné et al., 2018). Conversely, local approaches calibrate the parameter using local crack-tip fields such as strain maps obtained via Digital Image Correlation (DIC) (Loew et al., 2019) or the fracture process zone dimensions measured via SEM-based fractography (Darban et al., 2022). In the current study, the length scale parameter is calibrated by fitting the experimentally measured fracture load of Specimen 1. As will be discussed below, the calibrated length scale is of the same order of magnitude as the theoretically predicted size of the plastic zone ahead of the crack tip. Consequently, we postulate that this macroscopically calibrated length scale parameter also correlates with the dimensions of the local plastic zone at the crack tip.

The phase-field predictions of the fracture load (defined as the maximum load sustained by the specimen) for various values of the length scale parameter are presented in Fig. 10. As shown, increasing the length scale results in a reduction in the predicted fracture load. For a length scale of 1 mm, the phase-field model provides an accurate prediction of the experimentally measured fracture load. This value is used for the phase-field models in the next sections.

The calibrated length-scale parameter, $l_c = 1$ mm, is comparable to the size of the fully developed plastic zone ahead of the crack tip ($\theta = 0^\circ$) estimated using the von Mises yield criterion. For plane strain conditions $r_p^{strain} = (1-2\nu)^2 (K_{IC}/\sigma_Y)^2/(2\pi)$, and for plane stress conditions $r_p^{stress} = (K_{IC}/\sigma_Y)^2/(2\pi)$. Calculated from the data in Tables 3 and 5, the plastic zone sizes (r_p^{strain}; r_p^{stress}) are (0.38 mm, 3.71 mm) for the pure aluminum matrix, progressively decreasing to (0.20 mm, 1.76 mm), (0.09 mm,

Table 5
Simulation input parameters.

Material	Thickness [mm]	Young's modulus [GPa]	Poisson's ratio	Yield strength [MPa]	Hardening modulus [MPa]	Critical strain	Fracture energy [N/mm]
AlSi12	1.53	79.7	0.34	84	420	0.2	2.06
AlSi12+ 10%$A_{12}O_3$	1.37	92.4	0.33	118	940	0.07	1.66
AlSi12+ 20% Al_2O_3	1.48	110.2	0.31	150	2000	0.05	0.77
AlSi12+ 30% Al_2O_3	1.62	125.2	0.30	185	4500	0.02	0.61

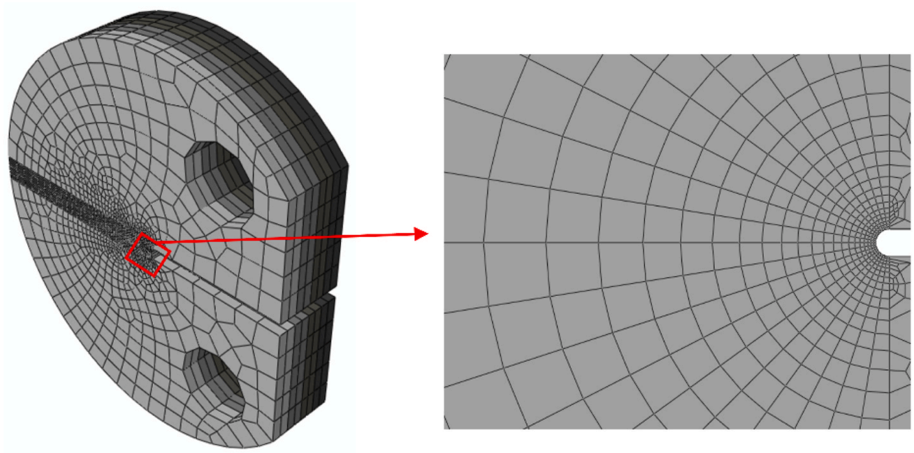

Fig. 9. Eight-node three-dimensional brick elements used for meshing of the specimen with fine mesh close to the crack tip, as shown in the inset.

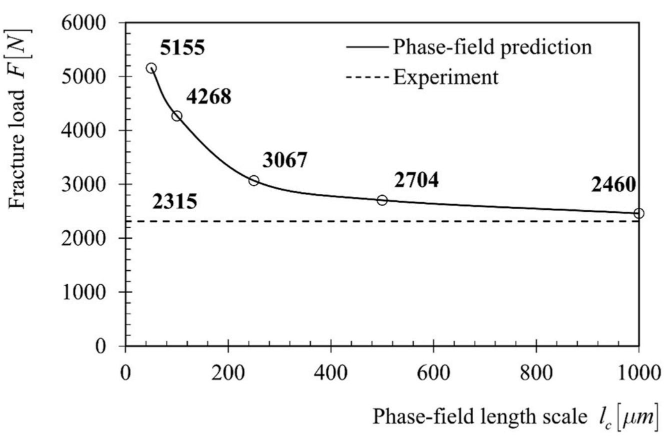

Fig. 10. Phase-field predictions of the fracture loads for different values of length scale parameters.

0.60 mm), and (0.06 mm, 0.36 mm) for the 10%, 20%, and 30% Al_2O_3 layers, respectively. Furthermore, comparing these dimensions with the microstructural analysis in Section 2.2 reveals that both the analytical plastic zone sizes and the calibrated l_c are one or two orders of magnitude larger than the individual particle sizes (2–10 μm, Table 1). This scale difference confirms that the crack tip interacts with a homogenized composite region rather than single particles, which physically justifies modeling each distinct layer as a homogeneous continuum with effective macroscopic properties.

The crack evolution, visualized by plotting regions where the phase-field parameter exceeds 0.99 at different load levels, is shown in Fig. 11. In agreement with the experimental observations in Section 2, the crack initiates within the layer containing 30 vol% reinforcement, which exhibits the lowest fracture toughness (see Table 3). As the applied displacement increases, the crack subsequently propagates into the layer with 20% reinforcement. With further loading, the crack reaches the third layer and develops a curved crack front. The crack penetrates the pure matrix layer only after a substantial development within the preceding layers. Notably, the crack front corresponding to 0.25 F_{max} exhibits features consistent with the experimentally observed crack front shown in Fig. 8. This correspondence provides additional confidence in the ability of the phase-field approach to reproduce both the global fracture response and the local crack path evolution.

The present phase-field modeling results demonstrate that, in a transversely graded composite containing a crack whose front is oriented along the graded direction, crack propagation occurs with a distinctly curved crack front. This behavior is consistent with analytical, numerical, and experimental studies reported in the literature for functionally graded and layered materials. In particular, the influence of elastic property gradients along the crack front on the variation of the stress intensity factor through the thickness was investigated in (Wadgaonkar and Parameswaran, 2009b), where it was shown that the classical square-root singularity of the crack-tip stress field is preserved despite the material gradation. However, the resulting thickness-wise variation of the stress intensity factor necessitates a nonlinear crack front evolution to satisfy local fracture criteria along the front. A similar conclusion was reached in (Kommana and Parameswaran, 2009), where an analytical expression for the through-thickness variation of the stress intensity factor was derived under simple bending conditions.

Experimental evidence supporting this mechanism was reported for layered epoxy/PMMA and Ti/TiB functionally graded materials. In single-edge-notched epoxy/PMMA specimens tested under three-point bending, crack growth was observed to initiate and propagate within the epoxy layer before the onset of crack propagation in the tougher PMMA layer (Bankar and Parameswaran, 2013). Similarly, bending and tensile tests on Ti/TiB graded beams showed that fracture initiated at the TiB-rich end and subsequently propagated toward the Ti-rich layer (Kidane and Shukla, 2010; Koohbor et al., 2019). Finite element simulations based on the XFEM framework further confirmed this curved crack-front evolution (Koohbor et al., 2019).

Fig. 12 highlights the contrasting fracture behaviors observed on the AlSi12 and AlSi12 + 30%Al_2O_3 sides of the graded material system. On the AlSi12 side, fracture proceeds in a ductile manner, which leads to plastic deformations near the crack edges. In contrast, the AlSi12 + 30% Al_2O_3 side exhibits fracture with sharp edges and limited plasticity, consistent with its higher reinforcement content and lower fracture toughness. The phase-field model adequately reproduces these distinct behaviors, capturing both the gradual damage accumulation leading to ductile failure in AlSi12 and the less ductile crack propagation observed in the AlSi12 + 30%Al_2O_3 layer. This is quantitatively supported by the simulated through-the-thickness displacement U_z (Fig. 12). On the pure matrix side, the numerical model predicts an inward displacement of approximately 160 μm at the crack edges, indicative of local plastic deformations. In contrast, this computed inward displacement is negligible on the AlSi12 + 30%Al_2O_3 side, confirming a highly localized, less ductile fracture.

To further investigate the interaction between the material gradation and the fracture response, the evolution of the equivalent plastic strain ahead of the initial crack is presented in Fig. 13. As the global load increases, an asymmetric plastic zone develops across the layers. The localized plastic strain first initiates in the AlSi12 + 30% Al_2O_3 layer

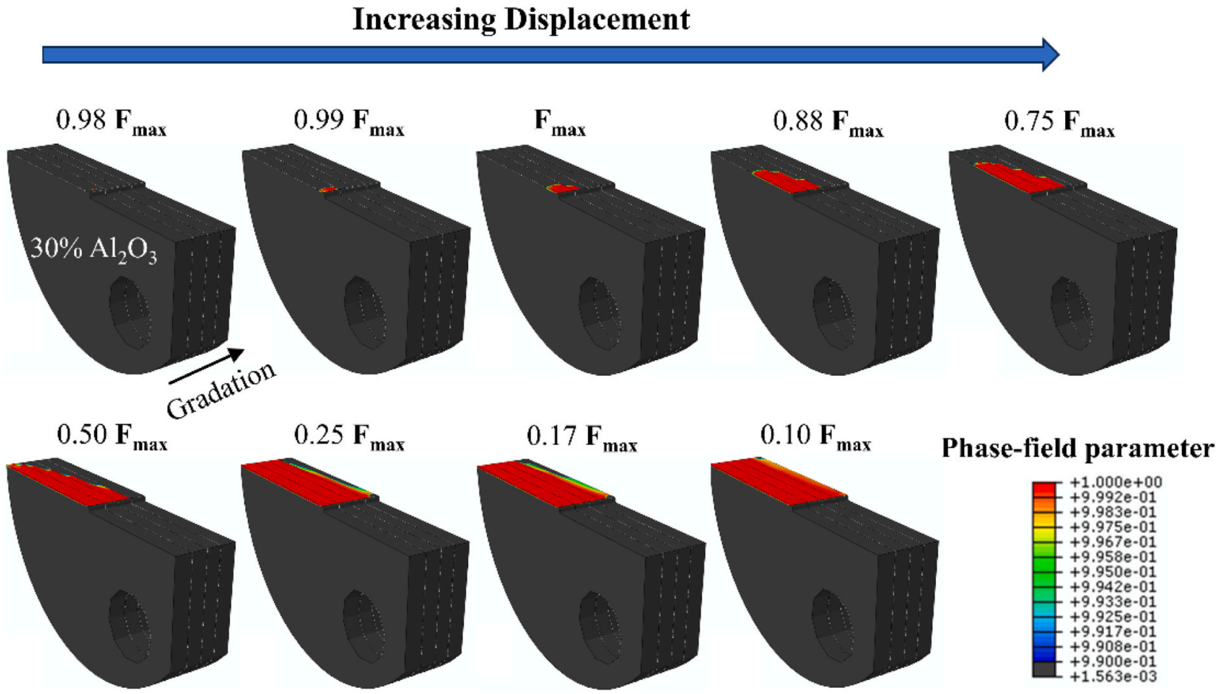

Fig. 11. Phase-field modeling results of the crack evolution in Specimen 1.

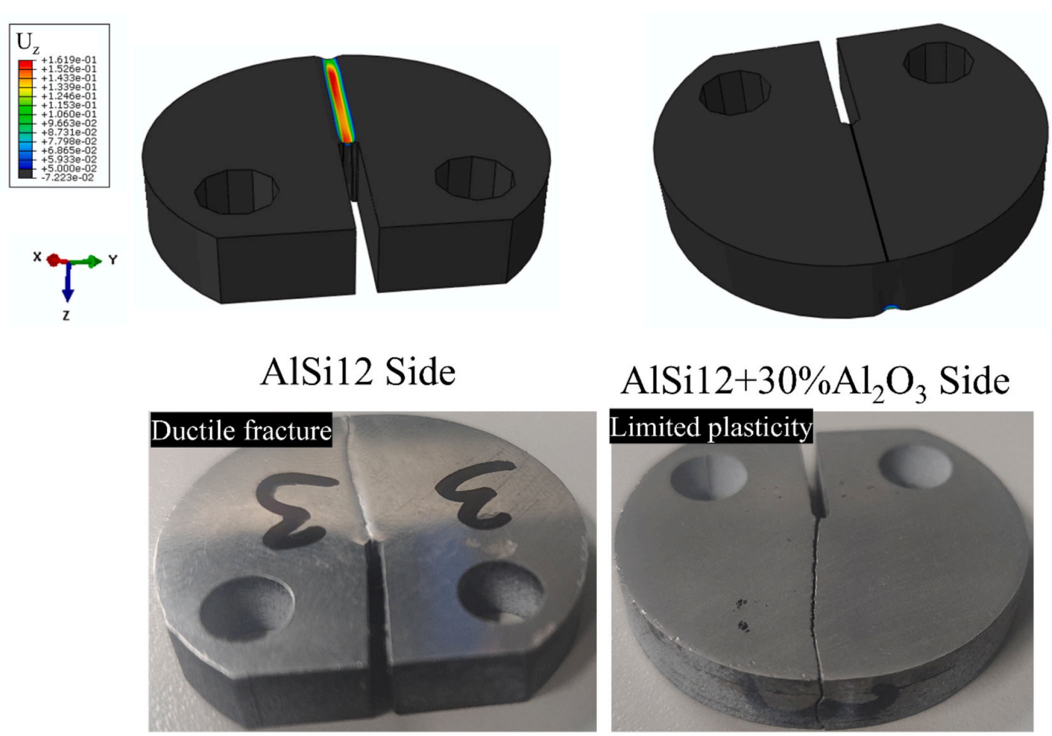

Fig. 12. Ductile fracture on the AlSi12 side and fracture with limited plasticity on the AlSi12 + 30%Al_2O_3 side. The phase-field prediction of the fracture on both sides is in agreement with the experimental observations. The color maps show the numerical predictions of the displacement in the thickness direction. (For interpretation of the references to color in this figure legend, the reader is referred to the Web version of this article.)

(denoted as "30" in the figure). However, this plastic zone does not develop significantly further since this layer has limited local plastic dissipation and a tendency toward brittle fracture. Conversely, in the more ductile layers (e.g., the unreinforced AlSi12 layer, denoted as "0"), the plastic zone expands significantly over time, yielding higher equivalent plastic strains within the layer. These numerical predictions are in agreement with the observations in Fig. 12, where macroscopic plastic deformation is visible on the pure matrix side, whereas the side containing 30% reinforcement exhibits a sharp, flat surface after fracture. The asymmetric plastic zone development contributes to the non-uniform crack front propagation (see Fig. 11), as the high ability of the pure matrix layer to dissipate energy through plastic deformation postpones local crack initiation.

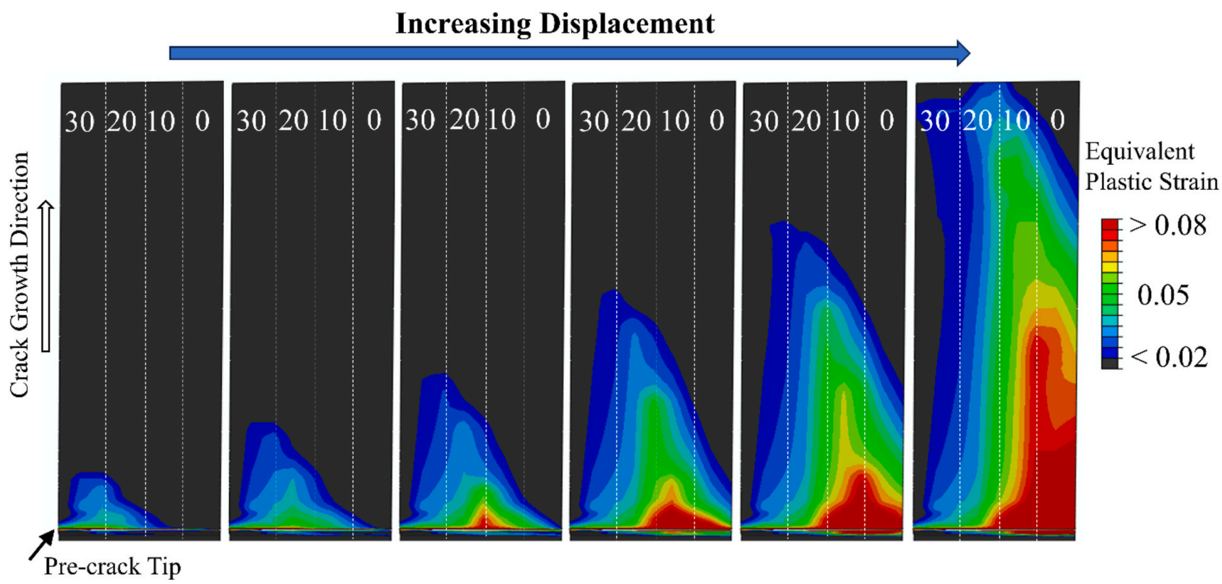

Fig. 13. Phase-field modeling results of the equivalent plastic strain evolution in Specimen 1.

3.2. Stacking sequence effect

Once the phase-field model is verified in the previous section, it is employed here to investigate the influence of stacking sequence on the load–displacement response and crack evolution. For consistency across cases, the thickness of each layer is set to 1.5 mm. The resulting load–displacement curves for the various stacking sequences are presented in Fig. 14. The loads and displacements are normalized by the fracture load and the corresponding displacement of the reference configuration, namely the [AlSi12/AlSi12 + 10%Al_2O_3/AlSi12 + 20% Al_2O_3/AlSi12 + 30%Al_2O_3] sequence (abbreviated as [0/10/20/30]). Four stacking sequences are examined by changing the position of the layer containing 30 percent reinforcement.

As shown in Fig. 14, the stacking sequence has a noticeable influence on the load–displacement response, including the maximum load capacity. The highest structural resistance is observed for the [30/0/10/20] and [0/30/10/20] configurations. This behavior can be attributed to the interaction between layers of differing fracture resistance and plastic deformation capacity. Specifically, when the layer with the lowest fracture toughness (AlSi12 + 30%Al_2O_3) is positioned adjacent to the most ductile layer (AlSi12), the latter can undergo significant plastic deformation and dissipate energy ahead of the crack tip. This plastic dissipation provides an effective shielding mechanism that delays crack initiation and propagation in the weaker layer. As a result, the composite system sustains higher loads before failure.

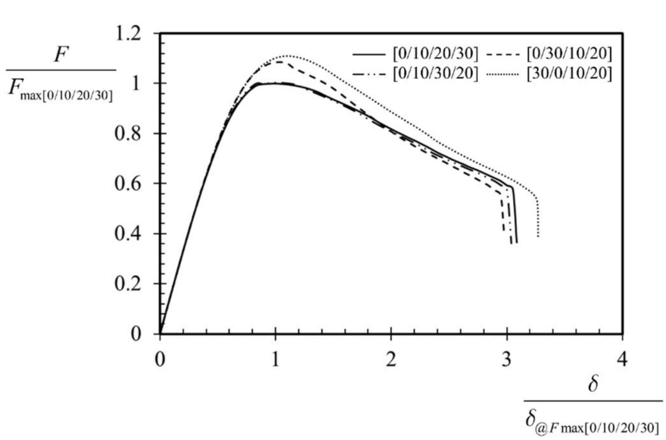

Fig. 14. Load–displacement curves for the different stacking sequences. The legend shows the percentage volume fraction of the ceramic in each layer. The loads and displacements are normalized by the fracture load and the corresponding displacement of the reference configuration, namely the [0/10/20/30] stacking sequence.

To provide further insight into the mechanisms underlying their distinct load–displacement responses, Fig. 15 illustrates the crack evolution for the four stacking sequences at selected stages of loading. In all configurations, crack initiation occurs within the layer exhibiting the lowest fracture toughness (AlSi12 + 30%Al_2O_3). However, the subsequent propagation path, the crack front geometry, and the rate of crack growth vary substantially with the stacking sequence. For sequences in which the 30 percent reinforced layer is placed adjacent to the more ductile AlSi12 layer, the crack front advances more slowly, and significant plastic deformation develops ahead of the crack tip, resulting in a more tortuous propagation path. This behavior is consistent with the enhanced load-bearing capacity observed for the [30/0/10/20] and [0/30/10/20] configurations. In contrast, when the weak layer is positioned away from the most ductile constituent, the crack advances more directly through the thickness. For all the considered cases, the crack front is curved with a unique geometry for each stacking sequence. The crack evolution patterns in Fig. 15 clearly demonstrate the crucial role of layer arrangement in controlling fracture resistance and energy dissipation in the graded composite.

The above layer-stacking analysis suggests that the different layers of this transversely graded AlSi12–Al_2O_3 FGM can trap macroscopic cracks due to varying local toughness along the crack front. This is similar to the layered and random toughness configuration cases studied by S. Roux et al. (2003).

3.3. Mixed-mode I/II loading

Fig. 16 presents the load–displacement response of the four stacking sequences under macroscopic mixed-mode I/II loading. To achieve this combined loading state, equal in-plane displacement components ($U_x = U_y$) are applied simultaneously along both the tension and shear directions, corresponding to an effective loading angle of 45°. Compared to the pure tensile case (pure mode I, Section 3.2), the maximum loads are generally lower across all configurations. This reduction occurs

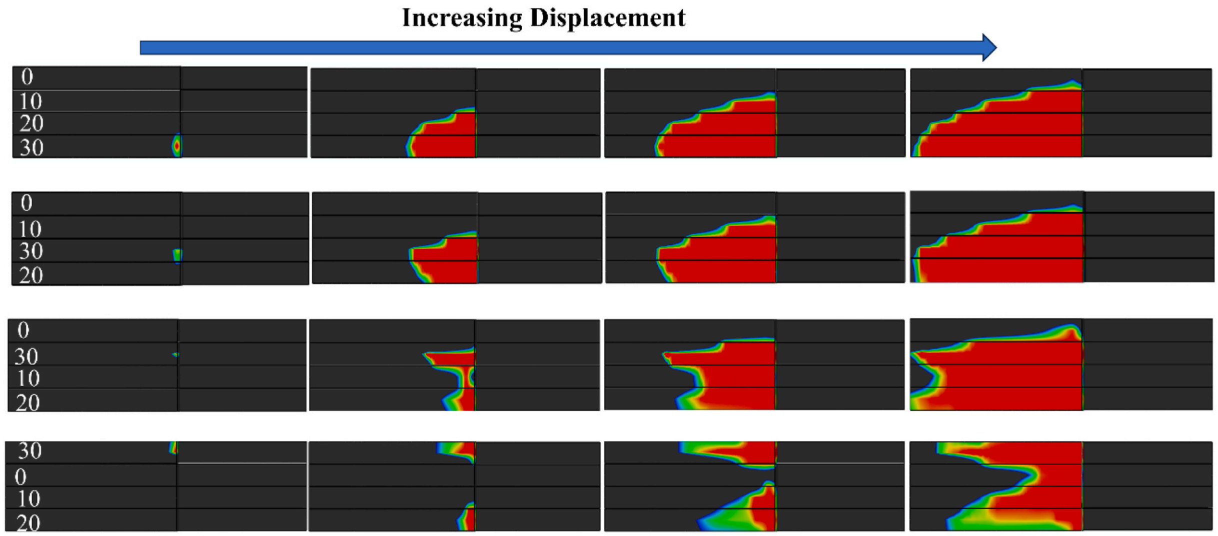

Fig. 15. The crack evolution for the four stacking sequences at selected stages of loading.

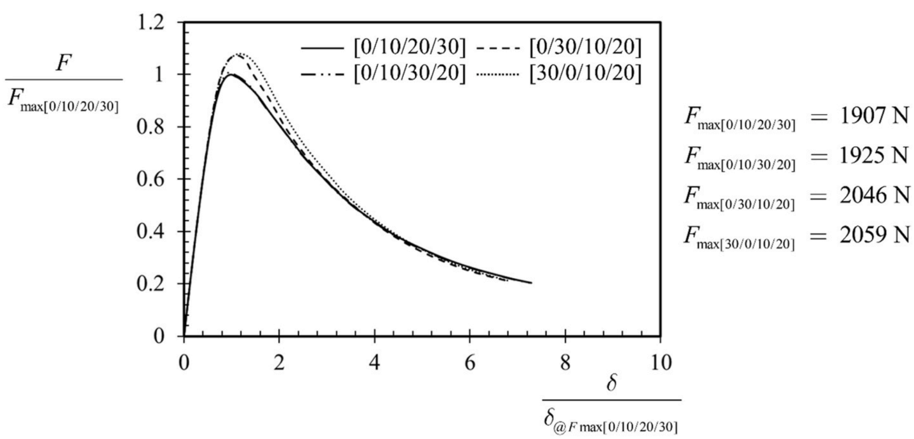

Fig. 16. Mixed-mode I/II load–displacement curves for the different stacking sequences. The legend shows the percentage volume fraction of the ceramic in each layer. The loads and displacements are normalized by the fracture load and the corresponding displacement of the reference configuration, namely the [0/10/20/30] stacking sequence.

because the presence of the shear stresses amplifies the stress levels at the crack tip, which promotes earlier crack initiation and propagation. The influence of stacking sequence remains noticeable: configurations in which the weakest layer (AlSi12 + 30%Al_2O_3) is adjacent to the most ductile layer (AlSi12) continue to exhibit higher load capacities. This is attributed to the same energy dissipation and shielding mechanisms observed in tension, where plastic deformation in the ductile layer delays crack advancement in the adjacent weak layer.

Fig. 17 shows the corresponding crack evolution for the four stacking sequences under mixed-mode I/II displacement. Mixed-mode loading introduces shear components that modify the crack trajectory, leading to an inclined crack growth path compared to the direct crack propagation in the pure tensile case. In sequences where the 30% reinforced layer is placed next to the ductile AlSi12 layer, the crack propagation remains slower, with pronounced plastic zones developing ahead of the crack tip. Also, for the mixed-mode loading, the crack front is curved with a unique geometry for each stacking sequence. These results highlight that the stacking sequence not only affects the load-bearing capacity but also significantly influences the mixed-mode fracture mechanisms and crack path morphology.

While the layer-wise mode mixity is not quantified, it is still possible to comment on the crack propagation behavior based on the specific material properties. Because the 30% reinforced layers exhibit predominantly brittle fracture, the crack preferentially propagates under local Mode I dominance. This Mode I dominance decreases as the reinforcement volume fraction is reduced and the layer transitions to a more ductile behavior. In the unreinforced pure matrix layer, which exhibits pronounced elastoplastic behavior, a non-negligible local Mode II component can be sustained. The elastoplastic phase-field model utilized in this study incorporates both tensile elastic and plastic strain energies into the damage-driving history field (see Appendix A and Eq. (A9)). In addition, the damage degradation function reduces the effective yield strength and hardening response as damage evolves (see Eq. (A5)). Consequently, plastic dissipation contributes directly to crack evolution, enabling the model to reproduce shear localization and the transition from tensile (Mode I) to shear-dominated crack propagation observed in ductile materials. However, mixed-mode fracture behavior is captured only indirectly, as the formulation does not include an explicit mode-mixity criterion, stress-triaxiality effects, or porous-plasticity mechanisms.

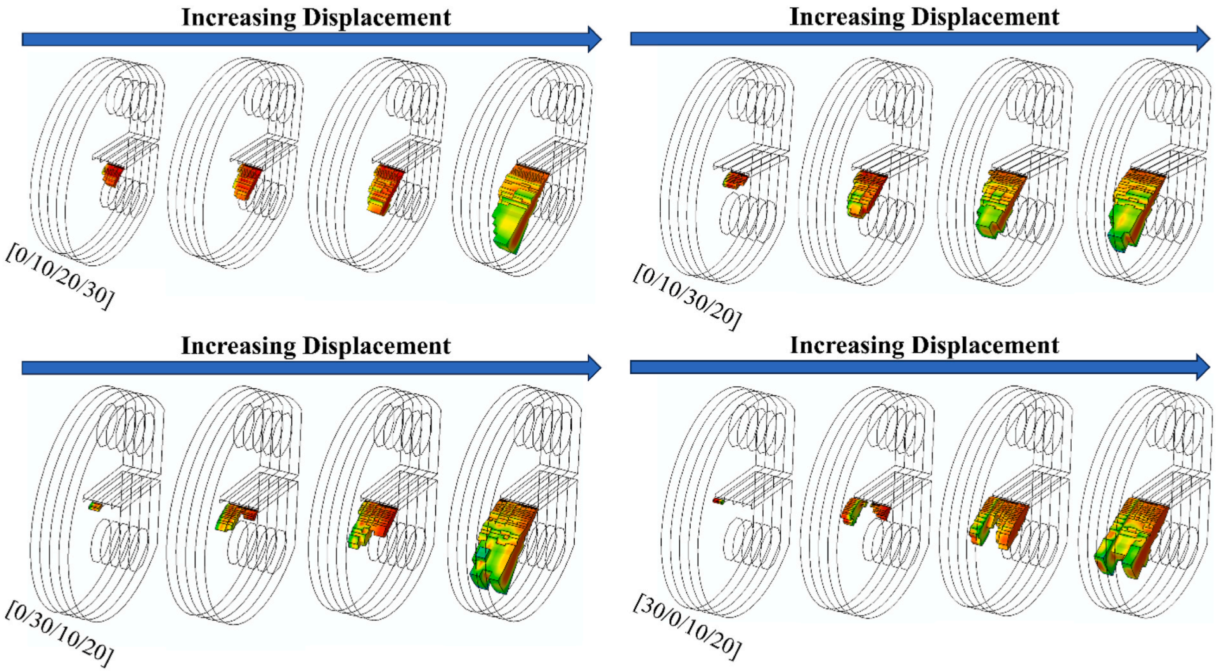

Fig. 17. The crack evolution for the four stacking sequences at selected stages of loading.

4. Conclusions

This experimental-modeling study focused on the fracture response of a transversely graded metal matrix composite (FGM) based on an aluminum alloy (AlSi12) matrix reinforced with aluminum oxide particles with varying volume fractions. The constituent and FGM samples used in the compact tension fracture tests were manufactured in-house via powder metallurgy to achieve high relative density. The focal point of this research lies in the examination of crack initiation and the growth trajectory, as influenced by the nonuniform distribution of fracture toughness along the crack front within a transversely graded system. The crack growth in the FGM compact tension specimen was monitored by a dual observation setup comprising a digital image correlation (DIC) system and a high-speed camera. It is confirmed that the ceramic reinforcements in the constituent composite layers play a pivotal role in fracture initiation and evolution of the FGM system. In parallel, the crack evolution in the FGM is studied by the phase-field elasto-plastic model, both in Mode-I and Mixed-Mode I/II loading. The shape and evolution of the crack front predicted by the phase-field model closely match the SEM fractography findings. The phase-field model results also reveal the significant impact of the layer sequence on the fracture behavior of the examined AlSi12–Al_2O_3 FGMs. The obtained results provide experimental and numerical insights into the fracture mechanisms of transversely graded metal matrix composites, thereby establishing design guidelines for the optimization of these materials.

Funding

The authors acknowledge the financial support of the National Science Centre, Poland, within research project no. 2019/35/B/ST8/03131. The European Virtual Institute on Knowledge–based Multifunctional Materials KMM-VIN AISBL is acknowledged for supporting the research stay of Hossein Darban at the Institute of Physics of Materials of the Czech Academy of Sciences (IPM, CAS) through the KMM-VIN Research Fellowship (Call 15).

CRediT authorship contribution statement

Kamil Bochenek: Conceptualization, Data curation, Investigation, Methodology, Validation, Visualization, Writing – original draft. **Hossein Darban:** Conceptualization, Formal analysis, Funding acquisition, Investigation, Methodology, Software, Supervision, Validation, Visualization, Writing – original draft. **Witold Węglewski:** Conceptualization, Funding acquisition, Investigation, Validation, Visualization, Writing – original draft. **Adam Brodecki:** Data curation, Investigation, Visualization, Writing – original draft. **Tomasz Katz:** Data curation, Investigation, Writing – original draft. **Ivo Dlouhy:** Data curation, Investigation, Validation, Writing – original draft. **Michał Basista:** Conceptualization, Formal analysis, Investigation, Methodology, Supervision, Validation, Writing – original draft.

Declaration of competing interest

The authors declare that they have no known competing financial interests or personal relationships that could have appeared to influence the work reported in this paper.

Acknowledgements

The authors gratefully acknowledge the Polish high-performance computing infrastructure PLGrid (HPC Centers: WCSS, ACK Cyfronet AGH) for providing computer facilities and support within the computational grant no. PLG/2026/019291. The authors would like to thank Mirosław Wyszkowski, from the Institute of Fundamental Technological Research of the Polish Academy of Sciences, for his technical assistance and expertise in designing and preparing the experimental setup for mechanical characterization.

Appendix A. Phase-field model formulation and implementation

The phase-field modeling results presented in Section 3 are obtained using the open-source Abaqus implementation developed in (Molnár et al., 2020). The model and its computer implementation are summarized below. For more details, see Ref (Molnár et al., 2020). and (Miehe et al., 2010).

In the phase-field model, a theoretical crack Γ within a 3D domain Ω, which is defined over a surface, can be approximated by the diffuse crack topology defined through the following volumetric integral:

$$\Gamma \approx \Gamma_{l_c}(d) = \int_\Omega \gamma(d, \nabla d) d\Omega = \int_\Omega \left[\frac{1}{2l_c} d^2 + \frac{l_c}{2}|\nabla d|^2\right] d\Omega \tag{A1}$$

where γ is the crack surface density function, and l_c and d are the phase-field length scale and parameter. The phase-field parameter d is zero in the undamaged and 1 in the fully damaged parts. The diffuse crack topology defined in Eq. (A1) allows for formulating the fracture problem as an energy minimization problem. To do so, the potential energy of the system is written as:

$$\Pi(\mathbf{u}, d) = E(\mathbf{u}, d) + P(\mathbf{u}, d) + W(d) \tag{A2}$$

where $\mathbf{u}$ is the displacement field. The terms on the right-hand side of the equation above are the elastic strain energy, the plastic strain energy, and the fracture energy.

Taking into account the fact that the material remains intact under pure compression, the elastic strain energy is given as:

$$\begin{aligned} E &= \int_\Omega \psi^{el}(\varepsilon^{el}, d) d\Omega = \int_\Omega \left[g(d)\psi_0^+(\varepsilon^{el}) + \psi_0^-(\varepsilon^{el})\right] d\Omega \\ \psi^{el}(\varepsilon^{el}, d) &= g(d)\left[\mu \sum_{i=1}^{3} (\varepsilon_i^{el})^2 + \frac{\lambda}{2}\langle tr(\varepsilon^{el})\rangle_+^{\,2}\right] + \frac{\lambda}{2}\langle tr(\varepsilon^{el})\rangle_-^{\,2} \end{aligned} \tag{A3}$$

with $\langle X\rangle_\pm = (X \pm |X|)/2$. λ and μ are the Lame coefficients. In Eq. (A3), ε^{el} is the elastic part of the total strain, while $tr(\varepsilon^{el})$ represents the mathematical trace of ε^{el}. The formulation is based on the small deformations assumption, where the total strain is given as $\varepsilon = \nabla^S \mathbf{u} = \varepsilon^{el} + \varepsilon^{pl}$, with ε^{pl} being the plastic strain. Additionally, $g(d) = (1-d)^2$ is the degradation function. The functions ψ_0^+ and ψ_0^- are the positive (tension) and negative (compression) parts of the elastic energy.

The second term on the right-hand side of Eq. (A2), the plastic energy, is defined as:

$$\begin{aligned} P &= \int_\Omega g(d)\psi_0^{pl}(\varepsilon^{pl}) d\Omega \\ \psi_0^{pl}(\varepsilon^{pl}) &= \varepsilon_{eq}^{pl}\left[\sigma^{\lim} + \frac{1}{2}H\varepsilon_{eq}^{pl}\right] + \frac{1}{2}I_\varepsilon \langle \varepsilon_{eq}^{pl} - \varepsilon_{eq}^{cr}\rangle_+^2 \end{aligned} \tag{A4}$$

where ε_{eq}^{pl}, $\sigma^{\lim}$, and H are the energy equivalent plastic shear strain, the von Mises yield strength, and the hardening modulus. The last term on the right-hand side of the second equation (A4) is a penalty term that assures the full degradation of the material at a given critical strain, ε_{eq}^{cr}. The penalty parameter I_ε is a high-value numerical coefficient that calibrates the rate of full degradation after the critical plastic strain is exceeded. Furthermore, the following von Mises yield criterion is implemented:

$$f(\sigma) = \sigma_{eq} - g(d)\left(\sigma^{\lim} + H\varepsilon_{eq}^{pl}\right) \tag{A5}$$

where σ_{eq} is the von Mises stress. The damage variable directly degrades the yield strength and hardening modulus (see the second term on the right-hand side of Eq. (A5)), allowing plasticity to physically guide the fracture path.

The fracture energy in Eq. (A2) is:

$$W = \int_\Gamma \mathscr{G}_c d\Gamma \approx \int_\Omega \mathscr{G}_c \gamma(d, \nabla d) d\Omega = \int_\Omega \frac{\mathscr{G}_c}{2l_c}\left(d^2 + l_c^2|\nabla d|^2\right) d\Omega \tag{A6}$$

where $\mathscr{G}_c$ is the fracture energy necessary for creation of a unit fracture surface.

To solve the coupled deformation and phase-field equations, an implicit, staggered finite element scheme is used (Molnár et al., 2020). Within this framework, a history variable $\mathscr{H}$ is introduced to establish a weak coupling between the deformation and phase-field problems, enabling the overall system to be evaluated iteratively as two separate, quasi-independent minimization tasks.

At each iteration, the solution starts with minimizing the energy of the deformation problem assuming a constant phase-field parameter defined at the previous iteration:

$$\prod^u = -E(u, d) - P(u, d) + \prod^{ext} \tag{A7}$$

where the last term refers to the work done by the body and boundary forces. Then, the phase-field problem is solved by minimizing the following functional:

$$\prod^{d} = \int_{\Omega} [\mathscr{G}_c \gamma(d, \nabla d) + g(d)\mathscr{H}] d\Omega \tag{A8}$$

with the history variable for the iteration n given as:

$$\begin{aligned} \mathscr{H}_n &= \max\left\{ \psi^{+}_{0,n-1} + \psi^{pl}_{0,n-1} \& \mathscr{H}_{n-1} \right\} \\ \mathscr{H}_0 &= 0 \end{aligned} \tag{A9}$$

Note that for the simulations presented in Section 3 of this manuscript, the asymmetric energy decomposition switch provided in the implementation by (Molnár et al., 2020) was disabled.

Appendix B. Crack geometry

The crack geometry implemented in the numerical model of Specimen 1 is shown in Fig. B1. The defect features a macroscopic primary notch (12.5 mm long and 1 mm wide) and a microscopic secondary notch with a semicircular tip. Because the microscopic notch depth and tip diameter (detailed in Table 4) differ slightly on each side of the specimen, average values were utilized for the simulation. To prevent artificial stress singularities, the boundary corners are rounded with a 0.1 mm fillet radius.

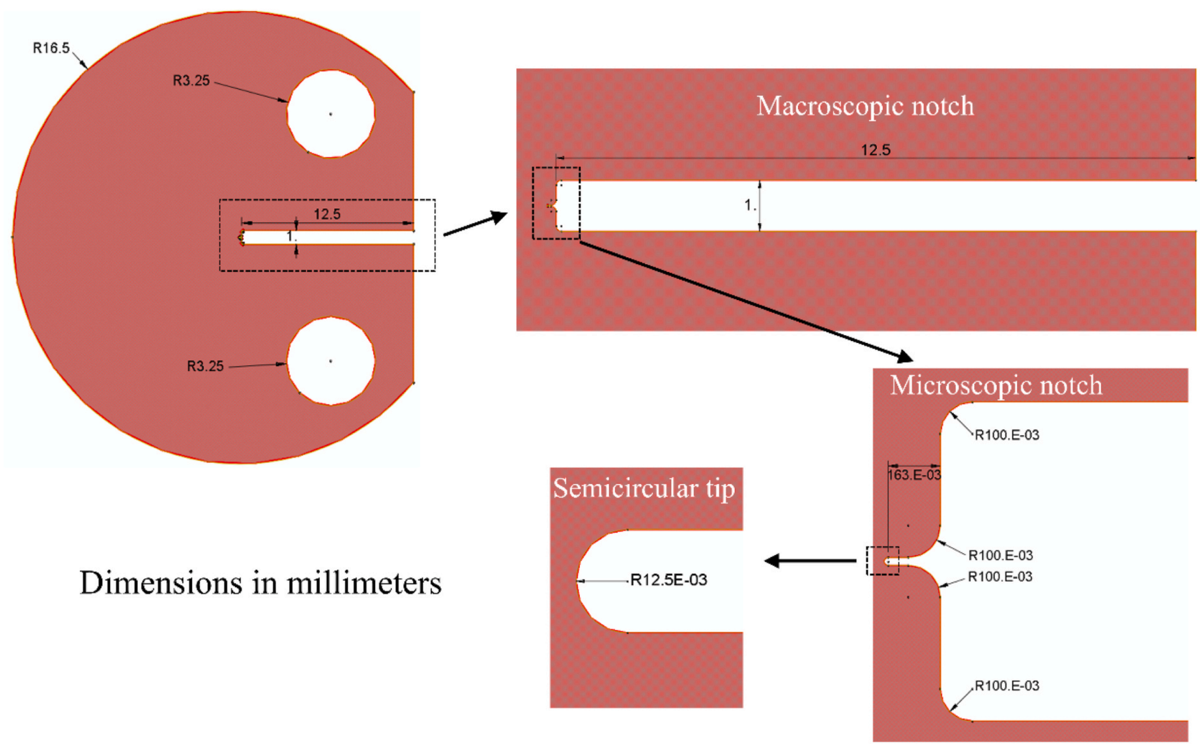

Fig. B1. Crack geometry and dimensions within the numerical model of Specimen 1 (see Fig. 4 and Table 4).

Appendix C. Convergence study

To verify that the use of two elements per layer provides sufficient numerical accuracy, a mesh convergence study was conducted by running additional simulations with four and six elements across the thickness of each layer. The resulting load–displacement curves and phase-field parameter distributions (crack trajectories) at approximately $F = 0.7\ F_{\max}$ are presented in Fig. C1. The loads and displacements are normalized against the peak fracture load and corresponding displacement of the two-element model. As evident from the figure, the predictions for all three discretizations are in excellent agreement, demonstrating that the results are independent of the mesh size in the thickness direction within the considered range.

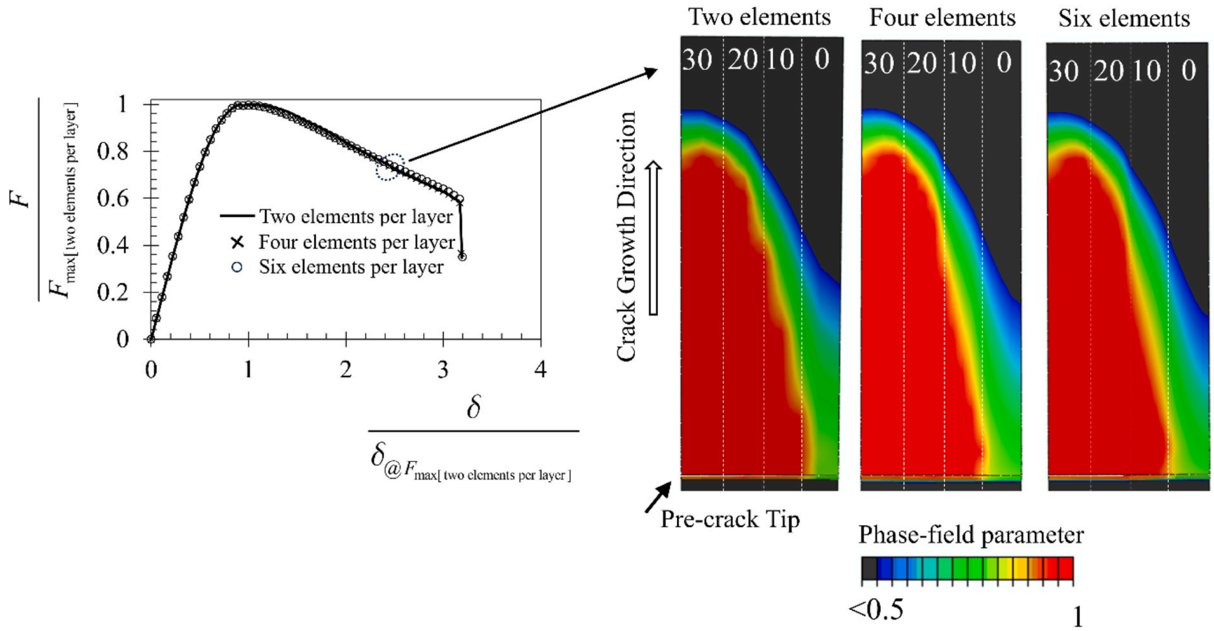

Fig. C1. Mesh convergence study: Load-displacement curves and phase-field parameter distributions (crack trajectories) at approximately $F = 0.7\ F_{max}$ for simulations using two, four, and six elements per layer.

Data availability

Data will be made available on request.

References

Anlas, G., Santare, M., Lambros, J., 2000. Numerical calculation of stress intensity factors in functionally graded materials. Int. J. Fract. 104, 131–143. https://doi.org/10.1023/A:1007652711735.

ASTM E 1820, 2001. Standard Test Method for Measurement of Fracture Toughness.

ASTM E399 – Standard Test Method for Plane-Strain Fracture Toughness of Metallic Materials, 2022.

ASTM E112-96, 2004. Standard test methods for determining average grain size. Reapproved 2004 e2 10–11.

Asur Vijaya Kumar, P.K., Dean, A., Reinoso, J., Lenarda, P., Paggi, M., 2021. Phase field modeling of fracture in functionally graded materials: Γ-convergence and mechanical insight on the effect of grading. Thin-Walled Struct. 159, 107234. https://doi.org/10.1016/j.tws.2020.107234.

Bankar, U.H., Parameswaran, V., 2013. Fracture of edge cracked layered plates subjected to in-plane bending. Exp. Mech. 53, 287–298. https://doi.org/10.1007/s11340-012-9649-6.

Basista, M., Jakubowska, J., Węglewski, W., 2017. Processing induced flaws in aluminum–alumina interpenetrating phase composites. Adv. Eng. Mater. 19, 1700484. https://doi.org/10.1002/adem.201700484.

Bochenek, K., Dlouhy, I., Węglewski, W., Chmielewski, M., Stepanek, R., Cupera, J., Pietrzak, K., Chmielewski, T., Morek, R., Basista, M., 2025. Fracture and wear behavior of high-chromium cast iron obtained from industrial waste and reinforced with alumina particles. J. Mater. Res. Technol. 37, 1579–1595. https://doi.org/10.1016/j.jmrt.2025.06.109.

Chak, V., Chattopadhyay, H., Dora, T.L., 2020. A review on fabrication methods, reinforcements and mechanical properties of aluminum matrix composites. J. Manuf. Process. 56, 1059–1074. https://doi.org/10.1016/j.jmapro.2020.05.042.

Darban, H., Bochenek, K., Węglewski, W., Basista, M., 2022. Experimental determination of the length-scale parameter for the phase-field modeling of macroscale fracture in Cr–Al_2O_3 composites fabricated by powder metallurgy. Metall. Mater. Trans. A 53, 2300–2322. https://doi.org/10.1007/s11661-022-06677-3.

Dinachandra, M., Alankar, A., 2020. A phase-field study of crack propagation and branching in functionally graded materials using explicit dynamics. Theor. Appl. Fract. Mech. 109, 102681. https://doi.org/10.1016/j.tafmec.2020.102681.

Doan, D.H., Bui, T.Q., Duc, N.D., Fushinobu, K., 2016. Hybrid phase field simulation of dynamic crack propagation in functionally graded glass-filled epoxy. Compos. B Eng. 99, 266–276. https://doi.org/10.1016/j.compositesb.2016.06.016.

Dolbow, J.E., Gosz, M., 2002. On the computation of mixed mode stress intensity factors in functionally graded materials. Int. J. Solid Struct. 39, 2557–2574. https://doi.org/10.1016/S0020-7683(02)00114-2.

Dsouza, S.M., Hirshikesh, Mathew TV., Singh, I.V., Natarajan, S., 2021. A non-intrusive stochastic phase field method for crack propagation in functionally graded materials. Acta Mech. 232, 2555–2574. https://doi.org/10.1007/s00707-021-02956-z.

Gayen, D., Tiwari, R., Chakraborty, D., 2019. Static and dynamic analyses of cracked functionally graded structural components: a review. Composites Part B 173, 106982. https://doi.org/10.1016/j.compositesb.2019.106982.

Ghanavati, R., Naffakh-Moosavy, H., 2021. Additive manufacturing of functionally graded metallic materials: a review of experimental and numerical studies. J. Mater. Res. Technol. 13, 1628–1664. https://doi.org/10.1016/j.jmrt.2021.05.022.

Gil, R., Jinnapat, A., Kennedy, A.R., 2012. Pressure-assisted infiltration of molten aluminium into open cell ceramic foams: experimental observations and infiltration modelling. Composites Part A 43, 880–884. https://doi.org/10.1016/j.compositesa.2012.02.001.

Gitter, R., 2008. Design of Aluminium Structures: Selection of Structural Alloys Structural Design According to Eurocode 9, Essential Properties of Materials and Background Information; Eurocodes-Background and Applications. Brussels, Belgium.

ISO 23146 Advanced Technical Ceramics - Test Methods for Fracture Toughness of Monolithic Ceramics - Single-Edge V-notch Beam, 2015. SEVNB) method.

Jin, Z.H., Noda, N., 1994. Crack tip singular fields in non-homogeneous materials. J. Appl. Mech. 61, 738–740. https://doi.org/10.1115/1.2901529.

Kidane, A., Shukla, A., 2010. Quasi-static and dynamic fracture initiation toughness of Ti/TiB layered functionally graded material under thermos-mechanical loading. Eng. Fract. Mech. 77, 479–491. https://doi.org/10.1016/j.engfracmech.2009.10.006.

Koizumi, M., Niino, M., 1995. Overview of FGM research in Japan, in functionally gradient materials. MRS Bull. 20, 19–21. https://doi.org/10.1557/S0883769400048867.

Kommana, R., Parameswaran, V., 2009. Experimental and numerical investigation of a cracked transversely graded plate subjected to in plane bending. Int. J. Solid Struct. 46, 2420–2428. https://doi.org/10.1016/j.ijsolstr.2009.01.026.

Koohbor, B., Rohanifar, M., Kidane, A., 2019. Characterizing fracture response of cracked transversely graded materials. Compos. Struct. 229, 111439. https://doi.org/10.1016/j.compstruct.2019.111439.

Li, Y., Feng, Z.Y., Hao, L., Huang, L.J., Xin, C.X., Wang, Y.S., Bilotti, E., Essa, K., Zhang, H., Li, Z., Yan, F.F., Peijs, T., 2020. A review on functionally graded materials and structures via additive manufacturing: from multi-scale design to versatile functional properties. Adv. Mater. Technol. 5, 1900981. https://doi.org/10.1002/admt.201900981.

Loew, P.J., Peters, B., Beex, L.A.A., 2019. Rate-dependent phase-field damage modeling of rubber and its experimental parameter identification. J. Mech. Phys. Solid. 127, 266–294. https://doi.org/10.1016/j.jmps.2019.03.022.

Madan, R., Bhowmick, S., 2020. A review on application of FGM fabricated using solid-state processes. Adv Mater Process Technol 6, 608–619. https://doi.org/10.1080/2374068X.2020.1731153.

Maj, J., Basista, M., Węglewski, W., Bochenek, K., Strojny-Nędza, A., Naplocha, K., Panzner, T., Tatarkova, M., Fiori, F., 2018. Effect of microstructure on mechanical properties and residual stresses in interpenetrating aluminum-alumina composites fabricated by squeeze casting. Mater. Sci. Eng., A 715, 154–162. https://doi.org/10.1016/j.msea.2017.12.091.

Miehe, C., Welschinger, F., Hofacker, M., 2010. Thermodynamically consistent phase-field models of fracture: variational principles and multi-field FE implementations. J Numer Methods Engrg 83, 1273–1311. https://doi.org/10.1002/nme.2861.

Miyamoto M (ed.) Functionally graded materials. Design, processing and applications. Materials Technology Series, Springer Science+ Business Media, New York, https://doi.org/10.1007/978-1-4615-5301-4.

Mohanty, S., Kumbhar, P.Y., Swaminathan, N., Annabattula, R., 2020. A phase-field model for crack growth in electro-mechanically coupled functionally graded piezo ceramics. Smart Mater. Struct. 29, 04500510. https://doi.org/10.1088/1361-665X/ab7145.

Molnár, G., Gravouil, A., Seghir, R., Réthoré, J., 2020. An open-source Abaqus implementation of the phase-field method to study the effect of plasticity on the instantaneous fracture toughness in dynamic crack propagation. Comput. Methods Appl. Mech. Eng. 365, 113004. https://doi.org/10.1016/j.cma.2020.113004.

Moore, P., 2014. The effect of notch sharpness on the fracture toughness determined from SENT specimens. Proceedings of the ASME 2014 33rd International Conference on Ocean, Offshore and Arctic Engineering. Volume 5: Materials Technology; Petroleum Technology. https://doi.org/10.1115/OMAE2014-24663. San Francisco, California, USA.

Mortensen, A., Suresh, S., 1995. Functionally graded metals and metal ceramic composites: part 1 processing. Int. Mater. Rev. 40, 239–265. https://doi.org/10.1179/imr.1995.40.6.239.

Neubrand, A., Rödel, J., 1997. Gradient materials: an overview of a novel concept. Int. J. Mater. Res. 88, 358–371. https://doi.org/10.3139/ijmr-1997-0066.

Nguyen, T.T., Yvonnet, J., Bornert, M., Chateau, C., Sab, K., Romani, R., Le Roy, R., 2016. On the choice of parameters in the phase field method for simulating crack initiation with experimental validation. Int. J. Fract. 197, 213–226. https://doi.org/10.1007/s10704-016-0082-1.

Niino, M., Hirai, T., Watanabe, R., 1987. Functionally gradient material- high temperature use for space rocket. J Jap Soc Compos Mater 13, 257–264 in Japanese.

Pandey, V.K., Patel, P., 2020. Study of quasi-static crack growth in aluminum/alumina functionally graded material using crack gauge. Theor. Appl. Fract. Mech. 110, 102777. https://doi.org/10.1016/j.tafmec.2020.102777.

Parameswaran, V., Shukla, A., 2002. Asymptotic stress fields for stationary cracks along the gradient in functionally graded materials. J. Appl. Mech. 69, 240–243. https://doi.org/10.1115/1.1459072.

Pradeep, A.D., Rameshkumar, T., 2021. Review on centrifugal casting of functionally graded materials. Mater. Today Proc. 45, 729–734. https://doi.org/10.1016/j.matpr.2020.02.764.

Roux, S., Vandembroucq, D., Hild, F., 2003. Effective toughness of heterogeneous brittle materials. Eur. J. Mech. Solid. 22, 743–749. https://doi.org/10.1016/S0997-7538(03)00078-0.

Sahragard-Monfared, G., Smudde, C.M., Carpenter, R.D., Munir, Z.A., Gibeling, J.C., 2023. Fracture resistance and crack growth mechanisms in functionally graded Ti–TiB. Metall. Mater. Trans. A 54, 3594–3602. https://doi.org/10.1007/s11661-023-07116-7.

Saleh, B., Jiang, J., Fathi, R., Al-hababi, T., Xu, Q., Wang, L., Song, D., Ma, A., 2020. 30 years of functionally graded materials: an overview of manufacturing methods, applications and future challenges. Composites Part B 201, 108376. https://doi.org/10.1016/j.compositesb.2020.108376.

Schneider, C., Rasband, W., Eliceiri, K., 2012. NIH image to ImageJ: 25 years of image analysis. Nat. Methods 9, 671–675. https://doi.org/10.1038/nmeth.2089.

Sequeira, A., Węglewski, W., Bochenek, K., Hutsch, T., Jain, A., Weissgaerber, T., Basista, M., 2024. Thermal conductivity of AlSi12/Al_2O_3-graded composites consolidated by hot pressing and spark plasma sintering: experimental evaluation and numerical modeling. Metall. Mater. Trans. A 55, 3706–3723. https://doi.org/10.1007/s11661-024-07506-5.

Sequeira, A., Węglewski, W., Bochenek, K., Hutsch, T., Jarząbek, D., Weissgaerber, T., Basista, M., 2026. Effect of SiC and Al_2O_3 reinforcements on the thermal conductivity of functionally graded AlSi12 matrix composites. Ceram. Int. 52, 6399–6415. https://doi.org/10.1016/j.ceramint.2025.12.394.

Sobczak, J., Drenchev, L., 2013. Metallic functionally graded materials: a specific class of advanced composites. J. Mater. Sci. Technol. 29, 297–316. https://doi.org/10.1016/j.jmst.2013.02.006.

Tanné, E., Li, T., Bourdin, B., Marigo, J.-J., Maurini, C., 2018. Crack nucleation in variational phase-field models of brittle fracture. J. Mech. Phys. Solid. 110, 80–99. https://doi.org/10.1016/j.jmps.2017.09.006.

Wadgaonkar, S.C., Parameswaran, V., 2009a. Structure of near-tip stress fields and variation of stress intensity factor for a crack in a transversely graded material. J Appl Mech, Trans ASME 76, 011014. https://doi.org/10.1115/1.2966177.

Wadgaonkar, S.C., Parameswaran, V., 2009b. Structure of near-tip stress field and variation of stress intensity factor for a crack in a transversely graded material. J. Appl. Mech. 76, 011014. https://doi.org/10.1115/1.2966177.

Zhang, C.H., Cui, M., Wang, J., Gao, X.W., Sladek, J., Sladek, V., 2011. 3D crack analysis in functionally graded materials. Eng. Fract. Mech. 78, 585–604. https://doi.org/10.1016/j.engfracmech.2010.05.017.

Zhang, X., Vignes, C., Sloan, S.W., Sheng, D., 2017. Numerical evaluation of the phase-field model for brittle fracture with emphasis on the length scale. Comput. Mech. 59, 737–752. https://doi.org/10.1007/s00466-017-1373-8.